Connectomics of the *Octopus vulgaris* vertical lobe provides insight into conserved and novel principles of a memory acquisition network

Authors

Flavie Bidel[1,*,+], Yaron Meirovitch[2,*,+], Richard Lee Schalek[2], Xiaotang Lu[2], Elisa Catherine Pavarino[2], Fuming Yang[2], Adi Peleg[2], Yuelong Wu[2], Tal Shomrat[3], Daniel Raimund Berger[2], Adi Shaked[1], Jeff William Lichtman[2], Binyamin Hochner[1,+]

[1] Department of Neurobiology, Silberman Institute of Life Sciences, The Hebrew University, Jerusalem, Israel

[2] Department of Molecular and Cellular Biology, Harvard University, Cambridge, MA, United States

[3] Faculty of Marine Sciences, Ruppin Academic Center, Michmoret, Israel

*Equal contribution.

[+]Corresponding Authors: bidel.flavie@gmail.com; yaron.mr@gmail.com; benny.hochner@mail.huji.ac.il

Summary

We present the first analysis of the connectome of the vertical lobe (VL) of *Octopus vulgaris,* a brain structure mediating acquisition of long-term memory in this behaviorally advanced mollusk. Serial section electron microscopy revealed new types of interneurons, cellular components of extensive modulatory systems and multiple synaptic motifs. The sensory input to the VL is conveyed via ~1,800,000 axons that sparsely innervate two parallel and interconnected feedforward networks formed by the two amacrine (AM) types, simple AMs (SAMs) and complex AMS (CAMs). SAMs make up 89.3% of the 25,000,000 AMs, each receiving a synaptic input from only a single input neuron on its non-bifurcating primary neurite, suggesting that each input neuron is represented in only ~12 SAMs. The CAMs, a newly described AM type, comprise 1.6% of the AM population. Their bifurcating neurites integrate multiple inputs from the input axons and SAMs. While the SAM network appears to feedforward sparse "memorizable" sensory representations into the VL output layer, the CAMs appear to monitor global activity and feedforward a balancing inhibition for "sharpening" the stimulus-specific VL output. While sharing morphological and wiring features with circuits supporting associative learning in other animals, the VL has evolved a unique circuit that enables associative learning based strictly on feedforward information flow.

INTRODUCTION

The advanced learning capabilities of cephalopod mollusks like *Octopus vulgaris* are comparable to those in some vertebrates (Sanders 1975; Mather 1995; Zarrella et al. 2015; Schnell et al. 2016; Hanlon and Messenger 2018). As the last common ancestor of cephalopods and vertebrates existed more than 500 million years ago (Packard 1972; Vitti 2013), the octopus provides a unique opportunity to study the independent evolution of nervous systems subserving sophisticated cognitive abilities (Hochner et al. 2006; Shomrat et al. 2015a; Hochner and Glanzman 2016; Turchetti-Maia et al. 2017). The vertical lobe (VL), the highest structure in the hierarchy in the central nervous system of the octopus, is regarded as a high order integrative center involved in visually evoked associative learning and memory acquisition (Boycott and Young 1955; Sanders 1975; Young 1979; Fiorito and Chichery 1995; Hochner 2010, 2012, 2013; Shomrat et al. 2015a; Shigeno et al. 2018; Turchetti-Maia et al. 2017). It is exceptionally large, containing 25 million neurons, about half the neurons in the central nervous system. This number is not much smaller than the number of neurons in the human hippocampus (~40 million, West and Gundersen, 1990) and about 4 orders of magnitude greater than the number of neurons in the mushroom body (MB) of *Drosophila* (e.g. Aso et al., 2014) and three orders of magnitude greater than that in the locust MB (Jortner et al. 2007).

Extensive neuroanatomical data on the VL were provided by the work of J. Z. Young and E. G. Gray in the 1960-70's using light and electron microscopy (Gray and Young 1964; Gray 1970; Young 1971). Based on estimated neuron numbers they proposed that the VL network is extremely simple, composed of only two types of morphologically distinguishable neurons: 25 million small amacrine interneurons (AM) and 65,000 large efferent neurons (LN). The main sensory input to the VL is conveyed via 1.8 million axons projecting from the median superior frontal lobe (SFL). These axons compose the SFL-VL tract that runs in the outer neuropil of the five VL lobuli. Each of these axons makes *en passant* synapses with a then unknown number of the AMs. These 25 million AMs converge sharply at a ratio of about 400:1 to innervate the LNs, whose axons were assumed to be the only output of the VL. Young pointed out that the pattern of SFL innervation of the AMs resembles the connectivity matrix in other learning and memory networks like the insect MB and the mammalian hippocampus (Young 1995).

This gross connectivity scheme provided insights that guided more recent physiological studies on the VL. Physiological experiments in the brain-slice preparation (Hochner et al. 2003, 2006) revealed that the *en passant* SFL-to-AM innervation is glutamatergic. It shows a robust activity-dependent NMDA-independent long-term potentiation (LTP) of glutamate release from the SFL presynaptic terminals (Hochner et al. 2003). The AM-to-LN connections are excitatory cholinergic synapses (Shomrat et al. 2011). Recently it was discovered that LTP at the SFL-to-AM synapse is maintained by a novel nitric oxide (NO)-dependent

63 ‘molecular switch’ mechanism in which NO switches ON NO-synthase (NOS) through a positive feedback
64 loop of NO-dependent NOS activation (Turchetti-Maia et al. 2018).

65 Although Gray and Young provided a detailed description of the main neuronal elements constituting the
66 VL network, the inability to reconstruct individual neurites limited the possibility of providing a detailed
67 circuit connectivity. Indeed, their observations reported unclassified cell types, thus suggesting that the VL
68 network is likely composed of more than the 3 neuronal elements they characterized (SFL, AMs and LN).
69 Previous findings in our group also hinted that the VL is more complex. Firstly, intracellular recording from
70 LNs revealed that some receive inhibitory inputs (Shomrat et al., 2011). Secondly, a recent wide-ranging
71 histolabeling study suggested that the AMs may be divided into at least two groups, one cholinergic and
72 the other GABAergic (Stern-Mentch et al. 2022).

73 To understand the octopus VL circuitry at a higher resolution the current study utilizes recent advances in
74 our ability to elucidate synaptic wiring diagrams at the nanoscale level using electron microscopy (EM).
75 Widely applied to various species and tissues this methodology has contributed much to understanding the
76 organization of neural networks (Kasthuri et al. 2015; Lee et al. 2016; Morgan et al. 2016; Ryan et al. 2016;
77 Motta et al. 2019; Li et al. 2020; Macrina et al. 2021; Meirovitch et al. 2021; MICrONS Consortium et al.
78 2021; Verasztó et al. 2020; Witvliet et al. 2021; Shapson-Coe et al. 2021). Here we sought to produce a
79 synapse-level wiring diagram of the *Octopus vulgaris* VL from serial EM by tracing out all pre- and
80 postsynaptic partners of dozens of main afferents of the VL (SFL projecting axons) and AMs. Indeed,
81 although we found that the gross anatomical organization of octopus VL fits the previous anatomical and
82 physiological model described above, the nanoscale analysis revealed new types of neurons and
83 connections that contribute profoundly to a deeper understanding of the functional organization of the
84 octopus VL and how it implements associative learning and memory.

85 Our data show that, firstly, in contrast to what was previously thought, the 25 million AM interneurons are
86 segregated into two distinct groups. The majority (~89.3 %) are simple AMs (SAM) that send a single non-
87 bifurcating neurite into the neuropil. A small fraction (~1.6 %) forms a very small group of newly
88 discovered complex AMs (CAM) with a branching dendritic tree. Secondly, we found that the SAMs
89 receive only one synaptic input from a single SFL axon. We propose that this synaptic connection may
90 serve as a “memory site” as it shows a robust activity-dependent LTP following tetanization of the SFL
91 axonal tract (Shomrat et al 2011). Thirdly, the segregated SFL-to-SAM expansion format suggests that
92 each of the 1.8 million SFL neurons is represented extremely sparsely in only around 12 of the 22.3 million
93 SAMs. Fourthly, in sharp contrast to the SAMs, the CAMs integrate dozen to hundreds of inputs,
94 suggesting that these interneurons integrate broader incoming SFL activity. As the SAMs and CAMs
95 converge onto the same output layer of LNs processes, our findings suggest the VL appears to be comprised

of two interconnected feedforward networks - one excitatory, originating from the SAMs (each representing one SFL) and a second, a parallel feedforward network, likely inhibitory, originating from the CAMs (each representing several SFLs). We demonstrated that distinct groups of SAMs and CAMs neurites fasciculate together to form a columnar organization in which each column constitutes canonical microcircuitry that may function as an "association module", associating SFL sensory features. Lastly, we described an additional afferent to the VL and two extrinsic putative neuromodulation systems. These interact with the feedforward networks and thus are likely involved in regulating the activity state of the network and in conveying reward and punishments signals.

RESULTS

The VL dataset and analysis

The region of interest (ROI) is in the lateral lobule of the VL (**Figure 1A**). We cut, collected and imaged 892 serial sections (30nm section thickness) at 4nm/pixel to generate a traceable 3D image stack covering a volume of 260x390x27 µm (**Figure 1B; Figure 1- video supplement 1**; 'connectome dataset' available at https://lichtman.rc.fas.harvard.edu/octopus_connectomes).

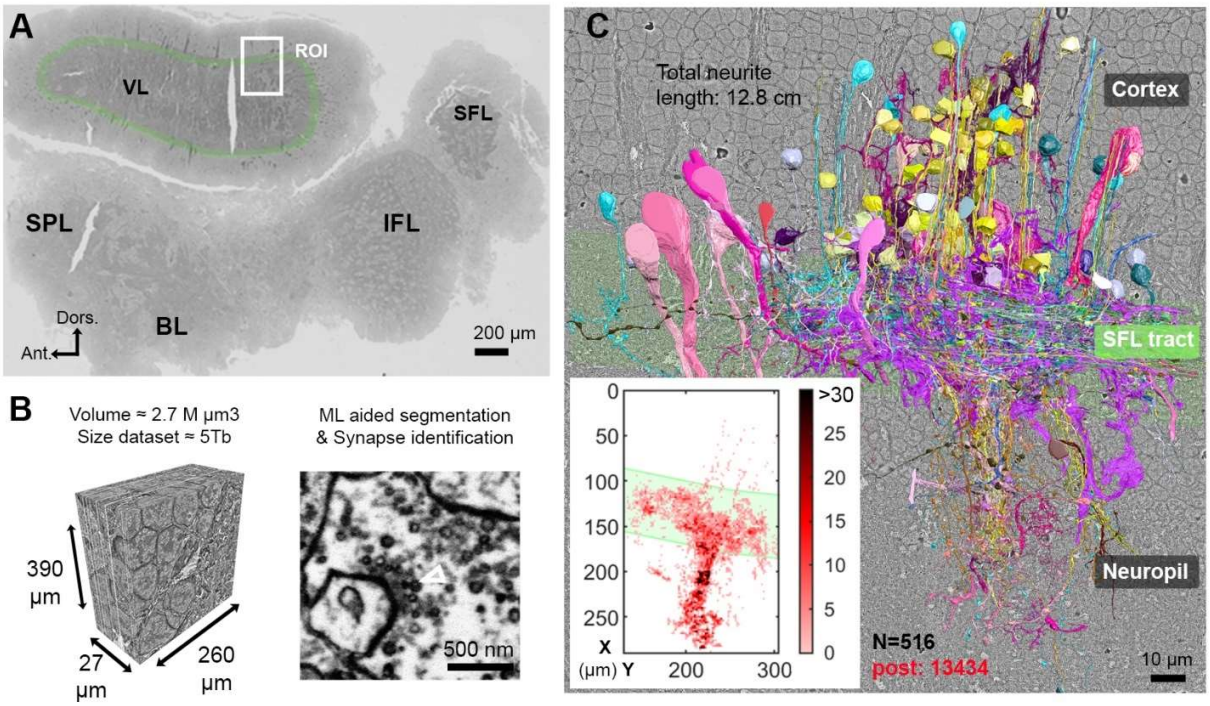

Figure 1. Reconstruction of octopus VL circuits using volume EM. (A) Low resolution image of the octopus central nervous system. The VL lies dorsally in the supraesophageal part of the central brain. The region of interest marked within it (ROI, white rectangle) was scanned with a scanning electron microscope (SEM) at 4 nm/px. (B) 30 nm sections were aligned in a traceable 3D stack (260x390x27µm. See also **Figure 1–video supplement 1**) for machine learning (ML)-aided by manual segmentation and synapse annotation. (C) The 516 reconstructed cell processes colored according to cell type (See **Figure 1–video supplement 2** for all cell types). Total neurite length of the reconstructed cells was 12.8 cm. Reconstructed cells are superimposed on a single EM image. Inset: spatial distribution of the 13434 postsynaptic sites annotated on the 516 cells presented as a heat-map. Abbreviations: BL, basal lobe; IFL, inferior frontal lobe; SFL, superior frontal lobe; SPL, subpedunculate lobe; VL, vertical lobe. See also **Figure 1–figure supplement 3** and **Figure 1–figure supplement 4**.

To classify the cells we used morphological features (*e.g.,* main neurite orientation, presence of varicosities, branching pattern), ultrastructural features (*e.g.,* vesicle size, mitochondria shape, cytoplasm staining, organelles) and connectivity assisted by the 'blueprint' established by Gray and Young (Gray and Young 1964; Gray 1970; Young 1971). Chemical synapses were identified based on features common to

127 invertebrate synapses - the presence of a cluster of synaptic vesicles (sv) or 'cloud' associated with an active
128 zone near the presynaptic membrane (Gray 1970; Ryan et al. 2016; White et al. 1986; Zheng et al. 2018;
129 Meinertzhagen 2019; Witvliet et al. 2021). Synapses were annotated if this accumulation of sv persisted
130 across at least three sections (> 90 nm). We classified synapses as fast chemical if the presynaptic
131 component contained sv of 30-60 nm diameter and modulatory synapses when the synaptic component
132 contained large vesicles (>60nm) (Messenger 1996; Leng and Ludwig 2008; van den Pol 2012; Witvliet et
133 al. 2020). Consistent with previous studies (Gray and Young 1964; Gray 1970), we did not observe any
134 obvious postsynaptic specialization (*i.e.,* postsynaptic density) at any chemical synapse and we found no
135 evidence of gap junctions.

136 We reconstructed 516 cell processes with a total length of 12.8 cm. The reconstructed cell processes were
137 classified into 10 cell types (**Figure 1–video supplement 2**) with 13,434 postsynaptic (**Figure 1C, heat**
138 **map**) and 2,472 annotated presynaptic sites. Among these 10 cell types, only 7 were involved in the VL
139 connectivity and therefore were analyzed in depth (see **Figure 1–figure supplement 3** for the 3 cell types
140 not discussed here). For characterization of the 7 cell types, we reconstructed throughout the volume at least
141 30 processes per cell type and annotated all their pre- and postsynaptic sites. Additionally, a subset of
142 cellular compartments and organelles (*i.e.,* cell bodies, nuclei and presynaptic varicosities) were separately
143 segmented to allow morphological quantification. The core of our connectivity reconstruction included
144 annotation and neurite reconstructions of all the synaptic partners of a subset of randomly selected 'seed'
145 cells (Morgan et al., 2016): SFL axons (35 of 84 SFL axons reconstructed) and SAM cells (28 of 108 SAMs
146 reconstructed).

147 We divided the analysis according to the three VL regions: 1) The outer cell body cortex; 2) the central
148 neuropil, and 3) the SFL tract, or outer neuropil, where axons projecting from the SFL are arranged in a
149 tract forming a ring around the outer zone of neuropil (Gray and Young, 1964; Young, 1971, Stern-Mentch
150 et al 2022). Note that because most of the cells are not fully contained in the reconstructed volume, it is
151 impossible to assess the full collection of synapses between pairs of neurons. We therefore used "synaptic
152 site" to refer to a single anatomical release site or a single synapse.

153 **The VL connectome is characterized by two parallel and interconnected feedforward networks**

154 **Figure 2** summarizes the 7 identified neuronal cell types and their connectivity (see also **Figure 2–figure**
155 **supplement 1**). None of the 84 reconstructed SFL axons bifurcated within the ROI (~260 µm long)
156 suggesting a very low rate of bifurcation of the SFL axons, if at all, as suggested by Young (1971). Each
157 SFL axon innervated *en passant* two distinct sub-populations of AMs; a very large population of
158 morphologically simple cells, which we termed 'simple amacrine' (SAM) and a small population of
159 morphologically complex cells that we termed 'complex amacrine' cells (CAM) (**Figure 2 and Figure 3**).

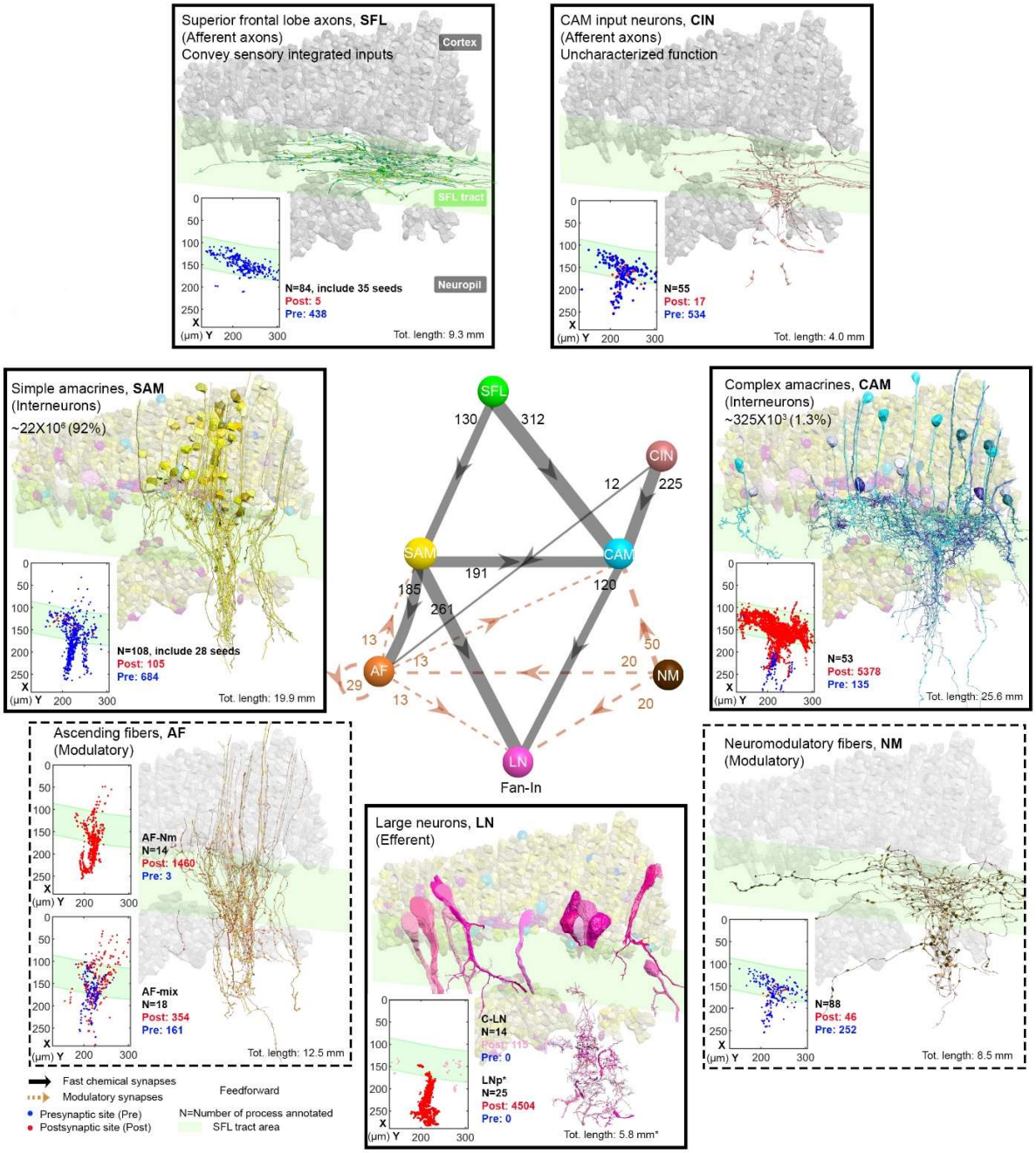

Figure 2. The 7 neuronal cell types classified in the ROI and their wiring diagram. The middle panel shows the wiring diagram, and the other panels depict the 7 neuronal cell types together with the spatial distribution of their postsynaptic sites (red puncta) and presynaptic sites (blue puncta). The approximate position of the SFL tract area (green) is shown for orientation and demarcating the outer from the inner neuropil. In the central panel each gray solid edge represents fast chemical synapses and the arrowhead the direction of these synapses; line width indicates relative number of synapses calculated from the number of connections annotated (noted next to each outgoing arrow). Orange dashed edges indicate chemical synapses observed with modulatory processes. Edges were represented only if more than 10 synapses were

169 annotated. Note that the connectivity is strictly feedforward ($p<0.05$). See **Figure 2–figure supplement 1**
170 for neurite level analysis.
171
172 The SAM and CAM cell bodies are intermingled in the cortex and their primary neurites run together in the
173 same bundles, also previously referred to as the *AM tract* (Gray and Young 1964; Gray 1970; Young 1979).
174 These bundles form a *quasi*-columnar organization toward the neuropil (**Figure 6A, 6B and Figure 7A**).
175 The SAMs and CAMs showed quite differed connectivity, morphology, and ultrastructure (**Figure 6A and**
176 **6B**). The SAMs are monopolar interneurons with a single non-bifurcating neurite. Their cell bodies are
177 small (mean ± std; 207.7 ± 26.1μm^3; n=69) and contain almost no cytoplasm. In contrast, the CAMs have
178 a complex bifurcating dendritic tree, a larger cell body (mean ± std; 337.2 ± 41.6 μm^3; n=16) and
179 cytoplasmic volume (**Figure 4**). Unexpectedly, we found that each SAM receives input from only one SFL
180 axon (See SAM section for details). In contrast, each CAM integrates synaptic inputs from a dozen to
181 hundreds of SFL axons and SAMs (**Figure 6B**). Both the CAMs and SAMs consistently converged onto
182 the LN processes (**Figure 7**). Overall, the transmission from the main afferents (SFLs) is entirely mediated
183 via the SAMs and CAMs into their shared target neurons - the dendritic processes of the LNs.

184 A second group of afferent axons innervated exclusively the CAMs. We termed these 'CAM-input-neurons'
185 (CIN; **Figure 8**). Even though CIN function has yet to be established, their ultrastructure is reminiscent of
186 the nerve endings which Gray and Young speculated may carry "pain" signals to the VL. They described
187 them as having neurofilaments ending shortly before the synaptic boutons which were filled with small
188 vesicles, a structure we also identified in our data. We also identified that the likely fast transmission circuit
189 (**Figure 2** panels framed with solid line) is overlaid by a diffuse mesh of two types of likely
190 neuromodulatory processes (NM and AF), each with a typical morphology, ultrastructure, and cell-specific
191 connections (**Figure 2**; panels framed with broken line). First, the 'neuromodulatory fibers' (NMs) manifest
192 a large variety of processes with large varicosities filled with large vesicles (60-200nm) that often do not
193 show the typical structure of a synaptic connection (detailed below). Second, the 'ascending fibers' (AFs)
194 climb from the neuropil up to the cortex through the *AM tracts* (i.e., a dense bundle of primarily SAM and
195 CAM neurites; **Figure 9**). A stereotyped feature of all AFs was their "menorah"-shaped bifurcating pattern,
196 close association with SAM neurites and their intense innervation by the SAM. The ultrastructure and
197 connectivity of these cells revealed two distinct subcategories, one likely neuromodulatory (AF-Nm,
198 **Figure 9C**) and the other yet undefined (AF-Mix, **Figure 9D**). Both the AF-Nm and the NM boutons were
199 filled with large vesicles and usually lacked synaptic outputs, suggesting that these are release sites of
200 neuromodulators or neuropeptides that are involved in extrasynaptic volume transmission (Bentley et al.,
201 2016). Since none of the AF and NM neurites were associated with a reconstructed cell body, we

202 hypothesize that AFs and NMs are external to the VL and may belong to the widespread ascending fibers
203 entering the VL from below that have been previously described (Young, 1971).

204 Overall, we show that the 7 cell types form a feedforward neural network in which only the AFs display
205 more than 10 reciprocal connections within a cell type (AF-to-AF, **Figure 2**). Analysis at the single neurite
206 level showed that the number of recurrent connections (cycles of connectivity) in the ROI was significantly
207 smaller than that in wiring diagrams built from the same set of neurites and synapses, but with otherwise
208 random directionality determining the pre- and postsynaptic neurons in each connection ($p<0.05$) (see
209 Methods). Moreover, the connections involved in feedback connectivity (*i.e.,* a cycle of connectivity) were
210 all associated with reciprocal connections which were rare.

211 **Each SFL axon innervates the SAMs and CAMs via two specialized bouton types**

212 A set of 35 seed SFL afferents was used for a detailed description of the connectivity pattern of the SFL
213 and its postsynaptic targets (**Figure 3A**). Each SFL axon was found to make two distinct types of synaptic
214 contacts depending on the target interneuron. First, an average of 28 ± 12 % (mean ± std) of the synapses
215 of each SFL axon (n=45/161, N=35 SFL) were made on SAMs (**Figure 3B** and **Figure 3–figure**
216 **supplement 1**). This synaptic connection is unique as each SAM received only a single SFL input. The
217 characteristic synaptic structure consisted of an especially large SFL bouton (LB, 6.41 ± 2.1 μm^3)
218 innervating *en passant* a specialized vesicle-filled postsynaptic compartment protruding from the SAM
219 primary neurite that partially wrapped the SFL LB (**Figure 3A, Figure 3–figure supplement 1** and **Figure**
220 **4**). We termed these postsynaptic structures 'palms' due to their somewhat flat and concave morphology.
221 Second, an average of 66± 11% of the synapses (109/161 synapses; N= 35 SFL) of each SFL axon were
222 made on CAM dendritic endings. These CAM endings were a variety of twig-like structures formed by
223 variably long (approximately 1 – 30 µm) thin protrusions emerging from thicker CAM dendritic branches
224 (**Figure 3A**). These postsynaptic profiles were electron-lucent and filled with polyribosomes (**Figure 3B**).

225 Unlike the single SFL-to-SAM connection, one SFL axon could make several synapses on the same CAM.
226 These SFL-to-CAM synapses showed two different arrangements. Either the synapses involved a large
227 presynaptic bouton (LB) of the SFL manifesting a multisynaptic glomerulus-like structure (**Figure 3A and**
228 **Figure 5**) or the synapses involved only a single CAM output with a significantly smaller presynaptic SFL
229 bouton (SB, 0.95 ± 0.88 μm^3; **Figure 3A**). The volume of all boutons (N=295) of all reconstructed SFL
230 axons (N=84) showed a bimodal distribution corresponding to these two different bouton types (**Figure**
231 **3C**).

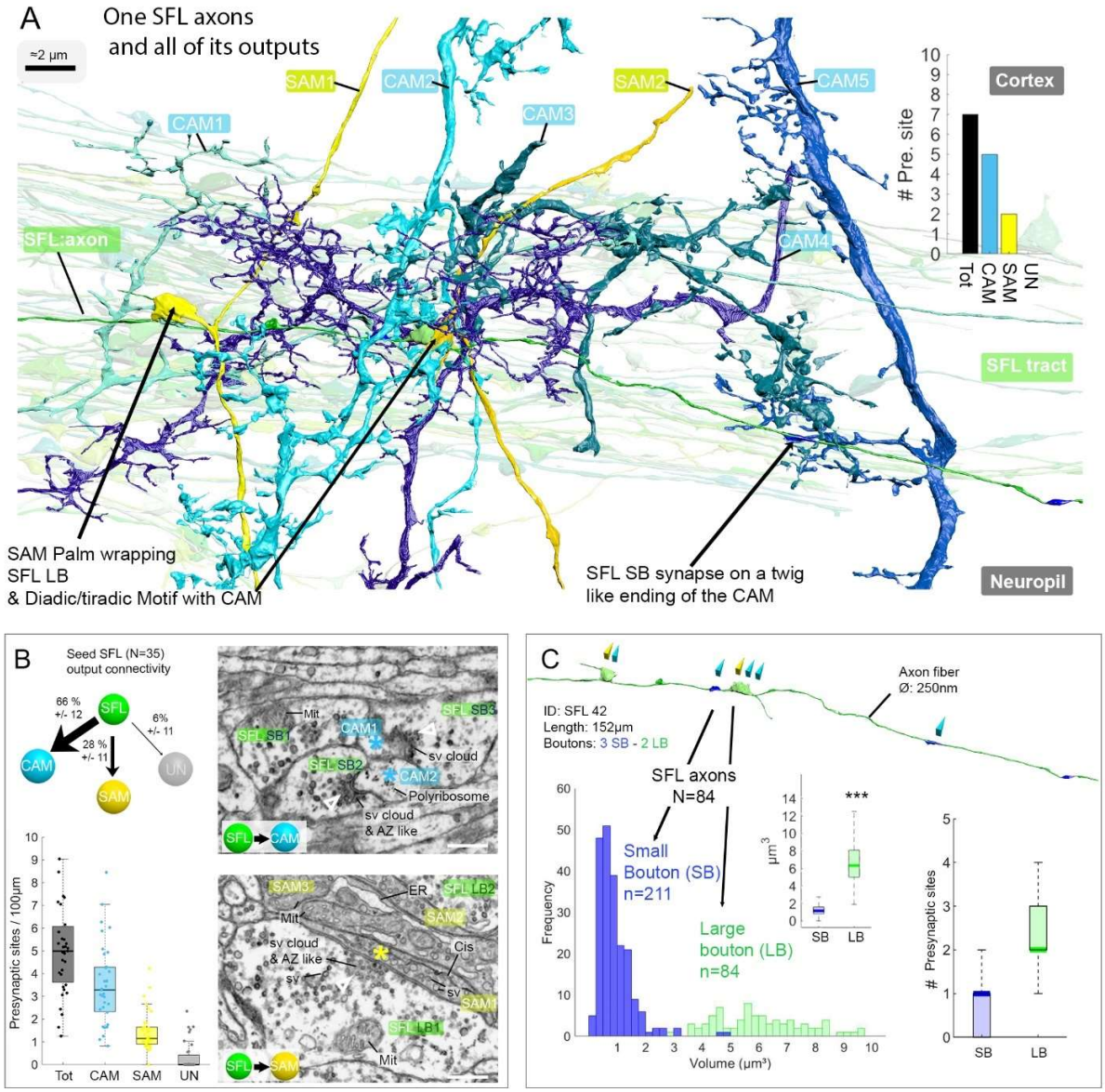

Figure 3. The SFL axons synapse onto the two populations of amacrine interneurons (SAMs and CAMs) via two distinct populations of presynaptic boutons. (A) Reconstruction of a single SFL axon (green) and its 7 *en passant* outputs within the reconstructed volume: 5 CAMs (various blue hues) and 2 SAMs (yellow). (B) Quantification of the synaptic outputs of the seed SFL axons (n=35) to SAMs (via large boutons; LB), CAMs (via small boutons; SB) and onto unidentified cell types (UN). Upper left shows distribution of connections in percent. On the right high resolution EM images of the SFL synaptic outputs onto SAM and CAM. 1nm/px, dwell time: 200 µs. Scale bar, 500 nm. Empty triangle and asterisk are respectively pre- and postsynaptic profiles. The whisker plot shows the relative density of the different presynaptic boutons along the 35 seed SFLs axons (C) Example of the distribution along an SFL axon segment of presynaptic outputs onto two SAMs (yellow triangles) and CAMs (light blue triangles). The histogram displays the bimodal distribution of bouton volumes of 84 SFL axons into two populations of small boutons (SB-blue) and large boutons (LB-green). The plot of presynaptic sites per SB and LB reveals

their monosynaptic and multisynaptic nature, respectively. Asterisks indicate statistical significance *** p<0.001, **<0.01. Abbreviations: sv, synaptic vesicles; AZ-like, active zone-like; Mit, mitochondria, Cis, cisternae; tER, transport endoplasmic reticulum. See also **Figure 3–figure supplement 1** and **Figure 3–video supplement 2**.

The number of CAMs is extremely low relative to that of SAMs

We were next interested in the relative abundance the SAMs and CAMs. Since we found significant differences in volume and shape of the various cell types, we reconstructed 1482 cell bodies without their projections and used volume and shape descriptors to build a Support Vector Machine classifier to estimate the number of different types of neurons in the VL (**Figure 4**).

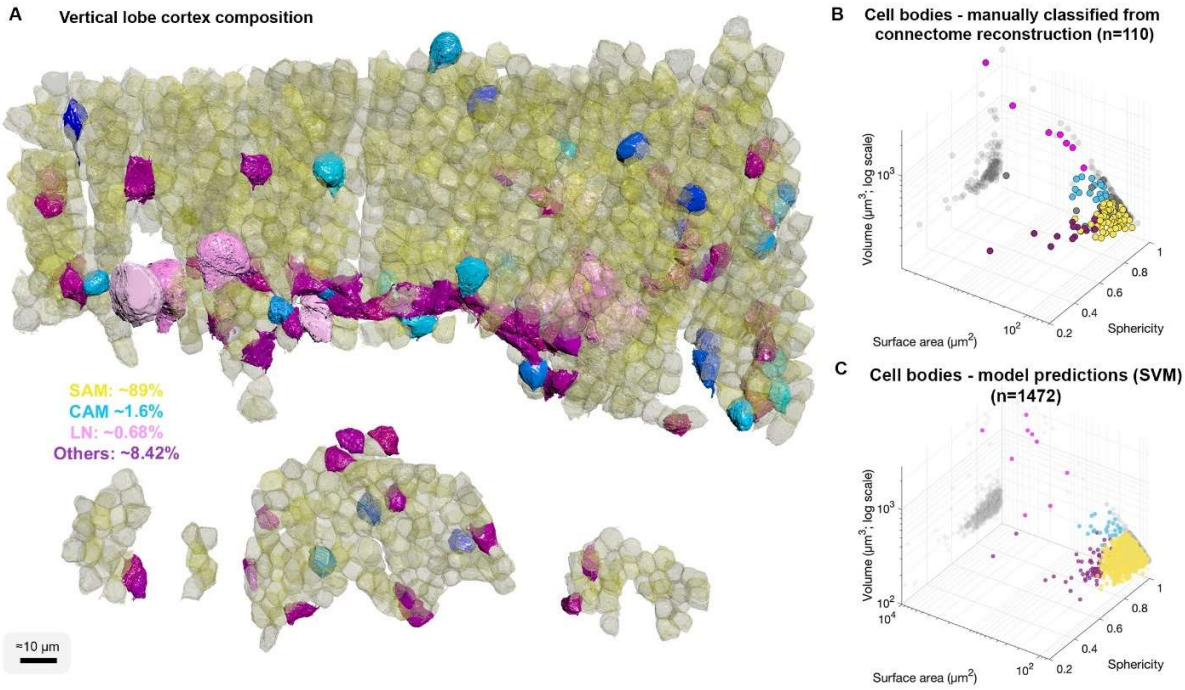

Figure 4. Cell body composition of VL cortex
A. A subset of 1472 densely packed cell bodies were reconstructed and automatically classified based on their morphology; SAM, yellow; CAM, blue hues; LN, pink; Others, purple. B-C. The classifier was designed to capture an observed correlation between cell type and cell body geometry roundish, relatively smaller cell bodies were associated with SAMs (vol 207.7 ± 26µm³, mean ± STD), often larger and slightly more elongated cell bodies with CAMs (vol 337.1671 ± 41.6 µm³), considerably larger cell bodies with highly variable volumes with LNs (volume range 464 – 2850 µm³), and elongated cell bodies with other cell types including glia and uncharacterized cells. A Support Vector Machine (SVM) was trained to separate 4 cell categories SAM, CAM, LN, and Others on a set of 110 manually classified cells based on 3 features: volume, sphericity, and surface area, and was validated on an independently prepared validation set with 47 cells (94.55% training accuracy with ~4.01% error on validation set all associated with SAMs).

We estimated that 89.3% of the cell bodies in the sampled volume were SAM cell bodies and 1.6% were CAMs (**Figure 4A**) with error rate on validation set smaller than 4.1% (see Methods). Assuming similar

proportions among all the 25 million AMs in the VL gives an estimate of ~22.3 ± 1.2 million SAMs and an estimate that the cortex contains fewer than 1.43M CAMs. As we did not observe any false negative or false positive associated with CAMs, the total number is likely close to the classifier's best estimate of 400,000 CAMs which can be further analyzed once this sparse set of cells is sampled on larger EM volumes. Assuming the SFL axons do not bifurcate in the MSF tract, then due to the one-to-one SFL-to-SAM innervation pattern the 1.8 million SFL axons fan-out onto the SAMs at an expansion ratio of about 1-to-12. Since each SAM is activated by a single SFL axon, then information from one SFL axon is represented at the SAM input layer in a non-overlapping manner in only about 12 ± 3.46 SAMs (assuming a Poisson distribution with an average of 12 LB). To estimate the distribution of LBs along the SFL axons we calculated the number of LBs per 100 µm in the 84 reconstructed SFL axonal segments. The results indicate an average and SD of 1.03 ± 0.73 LBs per 100 µm long segments suggesting highly sparse and variable (CV=0.77) distribution along the tract. If this distribution in maintained along large portions of the axon, then the LBs stretch over an average length of 1270 µm which grossly fits the length the of the SFL tract in our preparation (**Figure 1A**). This, in turn, suggests that the LB outputs into the 12 ± 3.46 SAMs is likely maintained along the entire length of the SFL axon rather than being confined in specific area.

The SAMs, CAMs and SFL large boutons are interconnected within synaptic glomeruli

The SAMs-to-CAMs connection forms the interconnection between the two parallel feedforward networks (**Figure 2**). These connections were found locally at a single large synaptic glomerulus encapsulating the SFL LB, the SAM palm and the CAM twig endings (**Figure 5**). Within this glomerulus these 3 neurons were repeatedly connected with multisynaptic motifs: monad, SFL-to-SAM (**Figure 5A**); dyad, SFL-to-CAM and SFL-to-SAM (**Figure 5B**), serial synapses, SFL-to-SAM-to-CAM, and triad where the same SFL presynaptic terminals innervate an adjacent SAM palm and a CAM twig ending (**Figure 5C**), as well as higher order polyads.

This arrangement fits the classical organization of synaptic glomeruli where a number of synapses are congregated in spatially compact structures, so that they may influence each other's functioning (Morgan and Lichtman 2020). Among these arrangements, the SAM palm, packed with vesicles, appears to be a unique bifunctional pre- and postsynaptic compartment, as most of the SAM palms formed serial synaptic connections (82%), receiving a synapse from a single SFL bouton and providing a synapse to 1 - 3 postsynaptic compartments, often twig endings of distinct CAMs. Analyzing a large population of 'long' SAM neurites (SAMs whose primary neurite was fully contained in the SFL tract area, N=56) revealed that each SAM exhibited only a single palm along its inwardly directed primary neurite (N=46/56), rarely two

palms (N=2/56) (**Figure 6C**) and each palm received input from only one SFL large presynaptic bouton (50/50 palms received a single SFL input).

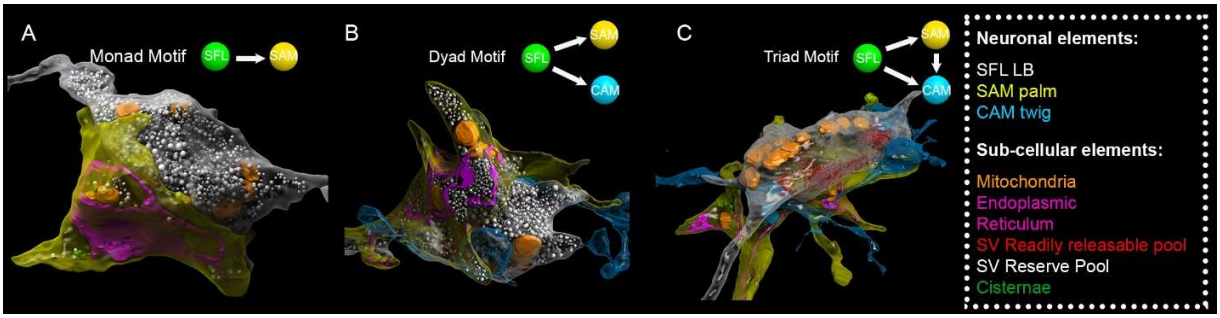

Figure 5. SFL large boutons (LBs) are found in multisynaptic motifs, forming a synaptic glomerulus involving serial connectivity with both SAMs and CAMs. Subcellular 3D reconstruction illustrating the main motifs involving the large varicosity of the SFL axon, which contains glutamate and makes *en passant* synapses. (A) monad (B) dyad and (C) triad. Note that in (C) only the readily releasable pool of synaptic vesicles is shown for clarity as otherwise the large "reserve" pool in the SFL LB (>5000 synaptic vesicles) would obscure other components of the image. The SFL LB were always partly wrapped by at least one SAM palm (yellow) and they often additionally synapsed onto a postsynaptic CAM twig-like ending (blue).

To better describe the structural properties of this unique palm structure we prepared a smaller dataset of 16x16x3.5 µm imaged at 1nm/px (high magnification dataset, see Methods). This revealed the complex presynaptic structure of the SAM palm which could contain up to 1500 synaptic vesicles (36.8 ± 7.7 nm) often tightly packed and resembling the "dense-walled" vesicles described by Gray and Young (1964). The structure included numerous elongated mitochondria and a large network of electron-lucent tubular organelles (**Figure 5**). These organelles could be small, disconnected units (cisternae, Cis) or large and continuous, likely part of the endoplasmic reticulum (ER). The main body of the ER usually faced the pre- and postsynaptic sites, possibly playing a role in vesicle recycling (Ramírez and Couve 2011; Weigel et al. 2021). We also occasionally observed what appeared to be exocytosis at the ER membrane, suggesting the possibility of a Golgi-like extended role in the synaptic vesicle machinery. It is still not clear whether the Cis (up to 15 observed in one palm) were part of the larger ER network or were isolated entities that could, for instance, play a role in keeping vesicles close to the active zone like synaptic ribbons (Dowling et al. 1966; Parsons and Sterling 2003) or the T-bar in Drosophila neurons (Scheffer et al. 2020).

The SAMs distribute their single SFL input onto the LNs, CAMs and AF

We next focused on a detailed reconstruction and proofreading of 28 SAM seed cells. As mentioned above, each seed SAM neuritic trunk received only one *en passant* SFL LB input (**Figure 6A**). The LB input was always located at the SAM palm (**Figure 5 and Figure 6A1, C**). Analyzing the neuritic trunks of SAM seed cells showed that 93% of the seed SAMs appeared to have no other inputs beside the SFL LB.

The SAM outputs were spread evenly along the length of the neuritic trunk. These synaptic outputs targeted 3 cell types (**Figure 6F**). As described by Young, (1971) and confirmed here, many SAMs converged onto the dendrite-like processes of the LN (LNp), mostly within the central neuropil but occasionally at the level of the SFL tract (**Figure 6A4 and Figure 6E**).

However, the SAM inputs to the LNp represented only 35% of the SAMs' presynaptic sites (N=109/271). The remaining connections are described here for the first time. 25% of the SAM outputs targeted the CAMs, while 26% innervated the processes of the climbing AFs, suggesting the SAMs directly innervate neuromodulatory processes. The SAM-to-CAM synapses were formed by a variety of dilatations of the SAM neuritic trunk containing clear, small vesicle-filled profiles synapsing onto a clear postsynaptic profile of the CAM twig (**Figure 6A2**). This was mainly observed within the SFL tract and in the upper neuropil. In contrast, the SAM-to-AF synapses (**Figure 6A3**) were spread throughout the dataset, including the cortex, and the postsynaptic element (AF) was a bouton often filled with dense-core vesicles (**Figure 9**). In the neuropil and the SFL tract these synapses were arranged in a rosette-like structure in which 2 to 5 adjacent SAMs synapsed locally onto the same AF bouton (**Figure 9**). Strikingly, within the cortex, the SAM soma occasionally synapsed onto AF varicosities, forming a heterodox somato-neuromodulatory synapse (**Figure 9A**). We also found rare cases of other synaptic outputs to NM (N=2/271), unidentified processes (N=19/271) and only one case of recurrent connection of a SAM onto itself (N=1/271) (**Figure 6F**). Reciprocal synaptic contact between SFL and SAM as well as AF and SAM were occasionally observed.

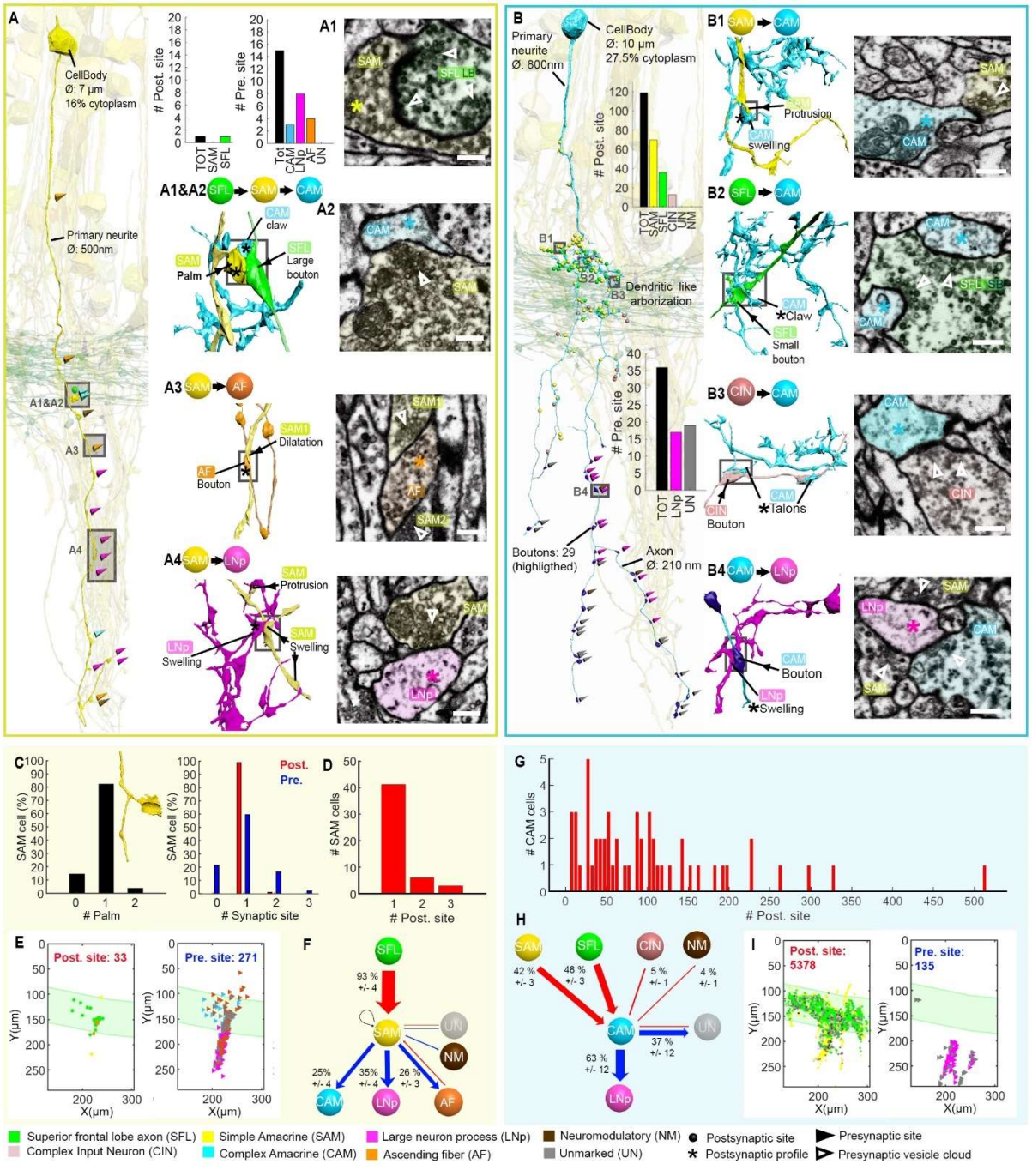

Figure 6. Stereotypic SFL ('mononeural')-input to the SAMs and multiple ('polyneuronal') inputs to the CAMs. (A,B) 2D projection of a reconstructed SAM (A) and CAM (B), superimposed on a reconstruction of the SFL tract (green). Triangles and puncta represent presynaptic output and postsynaptic input sites, respectively, color coded according to pre- or postsynaptic partner. The insets show the corresponding EM cross-section of each type of synapse. The morphological arrangement of the corresponding synaptic connection is depicted in the colored connectivity scheme next to each image and morphological reconstructions in the corresponding cells' color code (scale bar=500nm). (C) Analysis of the number of inputs onto the SAM 'palm' and its pre- and postsynaptic morphological specialization. 82%

363 of SAMs had only one palm, each receiving just one input (red bar). Each SAM innervated up to 3 targets
364 (blue bars). Only SAMs with their primary neurite fully contained in the SFL tract area were considered
365 (N=56). (D) The majority of the SAMs had only one input located at the palm. (E) Spatial localization of
366 the input/output of the 28 SAM seed cells within the ROI. Note the restriction of SFL-to-SAM inputs to the
367 area of the SFL tract. (F) The connectivity diagram of the 28 SAM seed cells shows the fraction of the
368 inputs (red) and outputs (blue) by neuron type. (G) Histogram showing the wide distribution of the number
369 of synaptic inputs to the CAMs (dozens to hundreds). (H) The connectivity diagram of 53 CAMs shows the
370 percentage of total inputs to and outputs from the corresponding cell type (color coded. See B1,2,3,4 for
371 details). Most of the CAMs' presynaptic partners were not reconstructed but identified based on
372 characteristic ultrastructure profiles. Profiles which could not be unambiguously identified were classified
373 as unidentified (Un). (I) Spatial distribution of the CAM inputs and outputs within the ROI. See also **Figure**
374 **6–figure supplement 1**, **Figure 6–video supplement 2**, **Figure 6–figure supplement 3** and **Figure 6–**
375 **figure supplement 4**.
376
377 **Morphology and connectivity of the CAMs**

378 The CAMs were probably not previously identified due to their small number relative to the huge number
379 of SAMs. Gray (1970) and Young (1971) may therefore have confused their dendritic arborizations and
380 electron-lucent ultrastructure within the SFL tract (**Figure 6A2,B1,B2 and B3**) with that of the LN. To
381 understand the potential functionality of these newly discovered interneurons within the VL circuitry we
382 annotated all their pre- and postsynaptic sites. Because the SFL, CINs, SAMs AFs and NMs all have
383 distinctive ultrastructure "fingerprints" (*e.g.,* cytoplasm staining, vesicle size, vesicle type, mitochondria
384 shape; see Methods), we were able to define their presynaptic partners without reconstruction.

385 The CAM neurites have 3 distinct regions: the *primary neurite* ramifies into strictly postsynaptic *dendritic*
386 *branches* in the SFL tract. The dendritic branches turn into neuritic *axons* in the deeper neuropil (**Figure**
387 **6B and Figure 6- figure supplement 2**). Synapses were located preferentially on numerous small twigs
388 which branched off the thicker dendritic branches. We used 'twig' to define CAM second-order dendritic
389 branches because their base lies on a microtubule-containing main thick branch(Schneider-Mizell et al.
390 2016) but, unlike spines that have a maximal length of less than 3 µm (Leiss et al. 2009), the twigs can be
391 much longer and show a complicated branching pattern. The CAMs showed variable dendritic branch
392 patterns and orientation, possibly suggesting the existence of CAM subtypes (**Figure 6- figure supplement**
393 **2 and 3**). Additionally, the morphology of the CAM twig endings was highly variable with at least 5
394 categories all somewhat resembling dendritic spine enlargements (**Figure 6B,C**): flatfoot, long neck
395 mushroom head, talon, palm-like and a claw-like endings that strikingly resembled the claw-like structure
396 wrapping the projection neurons in the insect MB (Leiss et al., 2009; Schürmann, 2016; Yasuyama et al.,
397 2002).

398 In contrast to the SAMs (**Figure 6–figure supplement 1**), each CAM interneuron received dozens to
399 hundreds of synaptic inputs (**Figure 6G and Figure 6–figure supplement 2 and 3**); the most extreme case
400 displayed 514 postsynaptic sites over a neurite length of 1.4µm. The CAMs integrate a combination of

401 inputs (**Figure 6H**), mostly from the SFL (48%, **Figure 6B2 and Figure 6–figure supplement 2G and**
402 **3E**) and the SAMs (42%, **Figure 6B1 and Figure 6–figure supplement 2F and 3F**). 5% of the inputs to
403 the CAMs originated from CINs (**Figure 6B3 and Figure 6H**). The CINs appeared to exclusively innervate
404 the CAMs with their inputs sparsely distributed over the CAM twig endings (**Figure 8**). Despite the CAMs
405 showing high diversity in primary neurite projection and dendritic arborizations, all received inputs and
406 innervated the same cell types and at similar locations within the VL (**Figure 6B and Figure 6–figure**
407 **supplement 3 and 4**). The CAMs' distal axonal processes innervated the LNps with many *en passant*
408 boutons (**Figure 6B4**).

409 **Different convergence patterns of SAMs and CAMs into the LNs**

410 Both the SAMs and CAMs converged onto the LNs, the output cells layer of the VL (**Figure 2, Figure 6**
411 **and Figure 7**). To investigate the pattern of LN innervation we first annotated all the synapses of 14 LNs
412 with reconstructed cell bodies and those on putative LN processes (see below, N=24). The LN cell bodies
413 (dia. > 15 µm) and their radially directed large primary neurite were poorly contained within our analyzed
414 volume. However, some of them (N=3/14) gave off dendritic collaterals within the SFL tract area where
415 they were solely postsynaptic to SAMs (**Figure 2**) and to other unidentified processes (with a total of 115
416 individual synaptic inputs on the LN processes in the SFL tract).

417 As suggested by the physiological experiments (Shomrat et al. 2011), we did not find any direct connections
418 between these LN dendritic collaterals and SFL axons. Among the 7 cell types thoroughly studied, we
419 consistently observed that the SFL, SAMs, CAMs, CINs, AFs and NMs processes all displayed an EM
420 profile filled with vesicles within the neuropil. Therefore, by elimination, we considered all electron-lucent
421 postsynaptic profiles within the neuropil as putative LN dendritic processes (LNp). The 24 LNps that we
422 examined branched profusely within the neuropil (**Figure 7A**) and were heavily innervated. The histogram
423 in **Figure 7D** shows that the LNps displayed the largest density of incoming synapses in the dataset with a
424 median of 162 postsynaptic sites/100 µm, far larger than the densely innervated AF-Nms (41 postsynaptic
425 sites/100 µm) and the CAMs (25 postsynaptic sites/100 µm that are restricted to the SFL tract; **Figure 7D**).
426 The SAM and CAM innervation of the LNps often formed rosette-like structures in which 2 - 5 or more
427 AMs made adjacent synapses onto an LN dendritic process (**Figure 7E**).

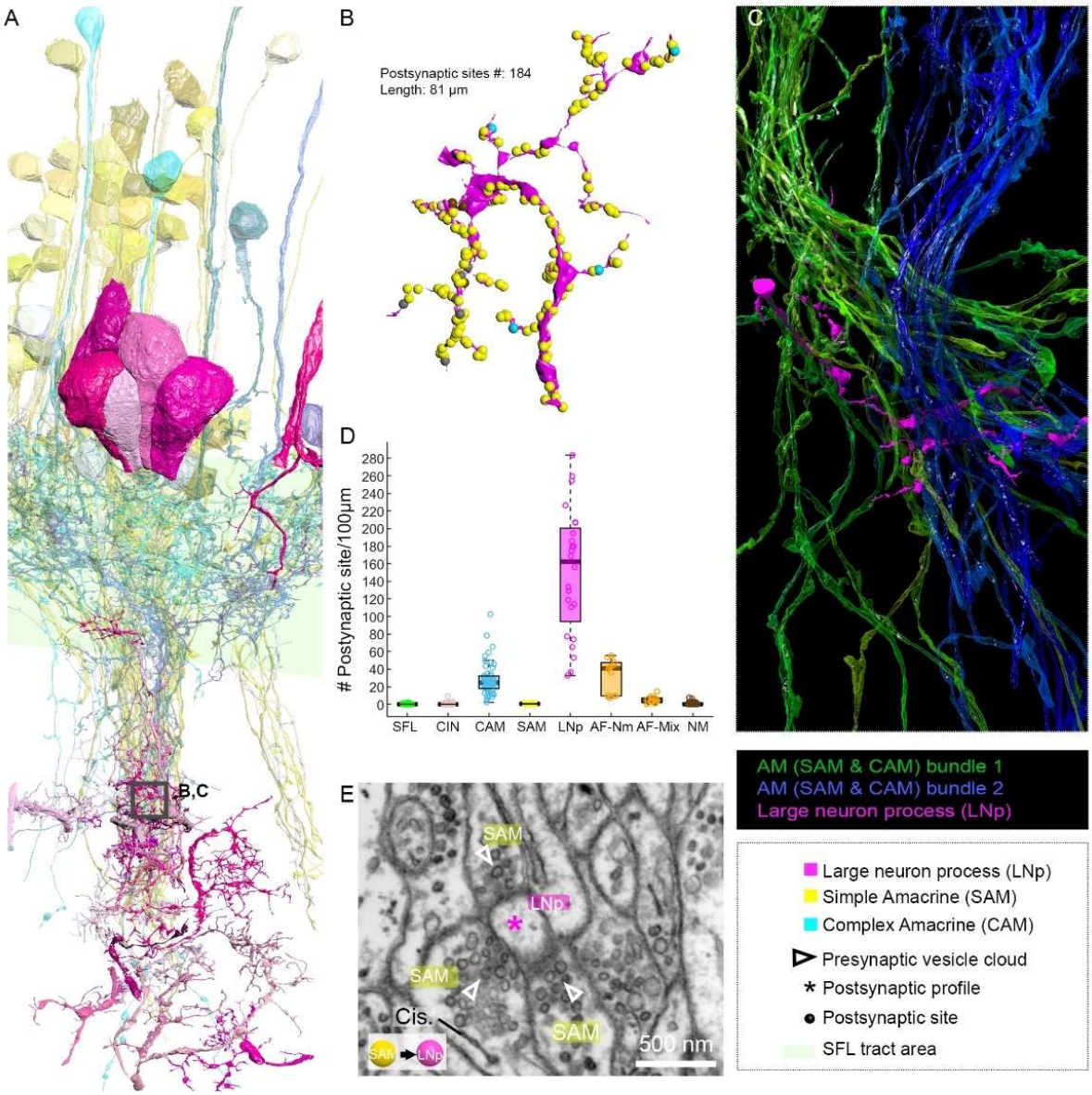

Figure 7. Patterns of synaptic convergence of SAMs and CAMs onto LNs. (A) 3D reconstruction of the LN cell bodies, and processes (LNp) (magenta hues) superimposed on SAMs (yellow) and CAMs (cyan). (B) Distributions of the 184 postsynaptic sites on one LN dendrite colored according to the legend. Note the very few CAM inputs relative to those of the SAMs. (C) Convergence of two bundles of intermingled SAM and CAM neurites onto an LNp shown in B. (D) The LNps displayed the greatest postsynaptic density among all dendritic elements. (E) High resolution EM illustrating a rosette-like structure formed by the convergence of 3 SAMs into one LNp. Empty triangle and asterisk are pre- and postsynaptic profiles, respectively. Resolution: 1nm/px. Dwell time: 200 µs.

We next estimated the degree of convergence of the SAMs and CAMs onto the LNs. For this we reconstructed and annotated all the neurites synapsing onto an 81 µm length of LNp dendrite (**Figure 7 B, C**). As shown in **Figure 7C** all the CAM and SAM inputs originated from two distinct fasciculate neuritic bundles (blue and green) that included 160 SAM neurites and only six CAMs. Approximately 90% of the

441 inputs on LNps were from SAMs (N=160/184 postsynaptic sites), only 3% were from CAMs (n=6/184
442 postsynaptic sites). **Figure 6B** shows that the CAM and SAM inputs were distributed in a "salt and pepper"
443 manner with the CAM inputs distributed very sparsely and evenly over the LN dendritic process. These
444 data indicate that the VL output neurons integrate massive information from the SAMs and only sparse
445 input from the CAMs. The spatial distribution of the CAM inputs to the LNp suggests a role of the CAM
446 output in adjusting the membrane potential of a large LN dendrite area. Such spatial distribution would be
447 most effective if the CAMs are inhibitory interneurons as we suggest below (see Discussion).
448

449 **The CINs afferents innervate exclusively CAMs**

450 CIN processes spread throughout the neuropil, but many ran parallel to the SFL axons (**Figure 8A**). Their
451 boutons were filled with many small, rounded mitochondria and the smallest vesicles observed in the VL
452 (≈30nm). Their presynaptic boutons displayed the greatest variability in size with volumes ranging from
453 0.09 to 29.50 μm^3 (median ± iqr; 1.65 ± 2.23).

454 Fifty-five of these fibers were reconstructed and their synaptic sites annotated. The CINs were almost
455 exclusively presynaptic (534 sites) with only very few postsynaptic sites (17 sites). All these presynaptic
456 sites were located on large boutons (N=239) that usually made polyadic synapses with several CAMs'
457 postsynaptic structures (*e.g.,* 3 in **Figure 8B** and 4 in **Figure 8C**) with a median of 2.3 ± 1.5 (median ± iqr)
458 synaptic sites per bouton (**Figure 8D**), the most extreme case being 8 presynaptic sites for a single bouton.
459 This synaptic structure may allow a single CIN terminal to influence several CAMs simultaneously.

460 The CIN innervate *en passant* mainly the CAMs (225 synaptic connections) and only occasionally the AFs
461 (**Figure 2 and Figure 2–figure supplement 1**). Note that the CAMs projected long thin side branches with
462 a morphological specialization at the tip (*i.e.,* long neck with mushroom head, **Figure 8C**) where it received
463 a synaptic input from the CIN bouton. The CINs displayed the highest presynaptic site density found within
464 the VL with a median of 11 presynaptic sites/100µm, twice as high as presynaptic density on SFL axons
465 (**Figure 8D**).

466

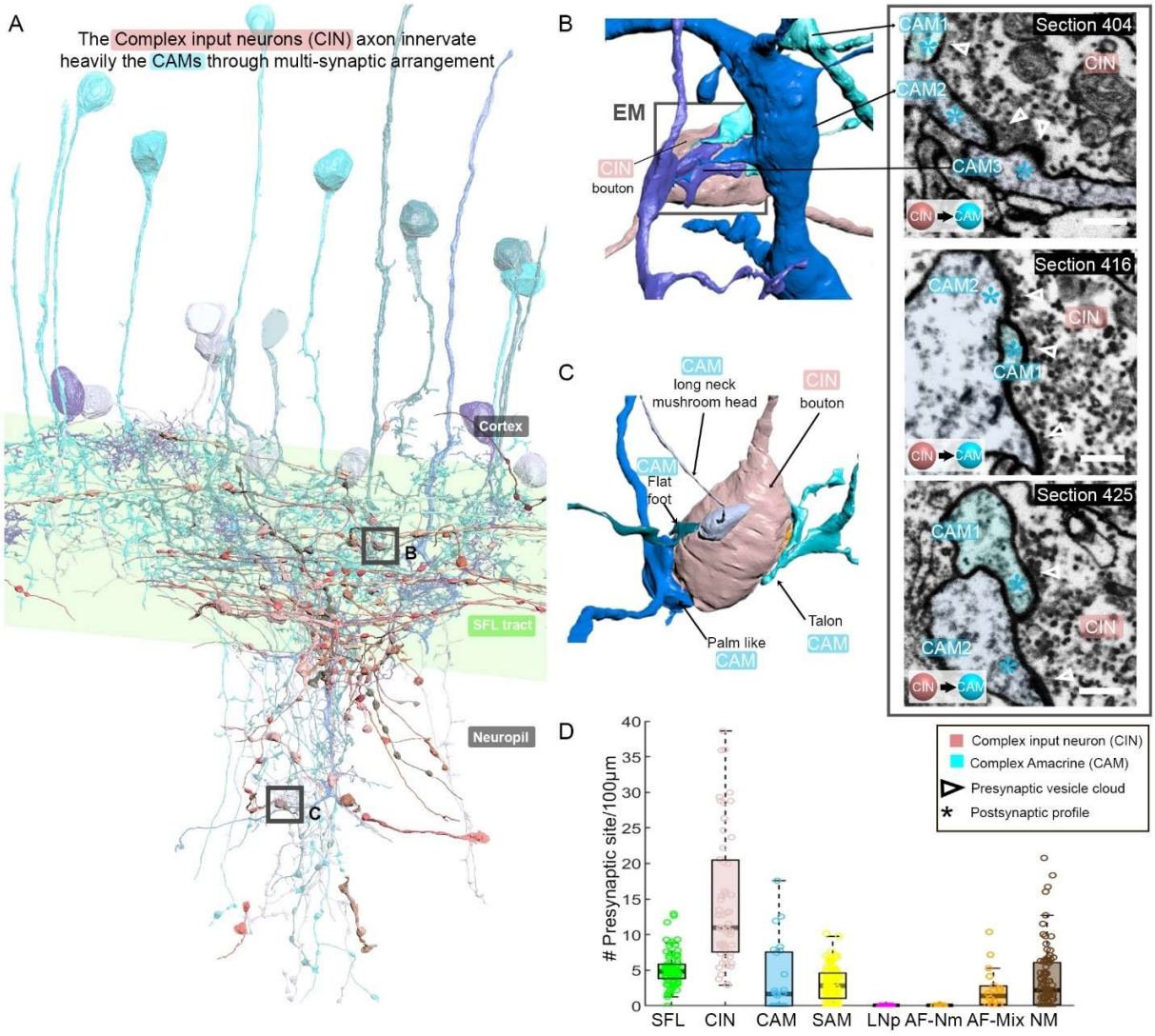

Figure 8. CAM-specific afferents (CINs) innervate exclusively CAMs via large multisynaptic boutons. (A) 3D reconstruction of a CIN (pink) superimposed on the CAMs, their main postsynaptic partners (blue hues). (B, C) 3D arrangement of a large CIN presynaptic bouton innervating multiple CAM dendrites (3 in B; 4 in C). CAM twig endings varied in shape resembling flattened dendritic spine enlargements. As indicated in C their structure can be divided into at least 5 classes. Right inset, 3 consecutives near cross-sections through a CIN bouton and its 3 postsynaptic targets. The CIN profile contained the smallest vesicles, about 30nm dia., of the entire dataset. (D) CIN had the highest presynaptic site density of the dataset. Error bar=SEM.

The neuromodulatory ascending fibers (AF) receive massive synaptic inputs from the SAMs

The AF were highly recognizable in our dataset with their menorah shape, climbing through the neuropil into the cortex while intermingling with SAM and CAM neurites (**Figure 9A**). Their processes displayed large boutons along their length (9.4 boutons/100µm). The reconstruction of the synaptic partners of the SAM seed cells revealed that the AFs receive massive input from the SAMs (**Figure 6F**).

481 Mapping the AF synaptic sites revealed two clear subcategories of AF based on their connectivity (**Figure**
482 **9B**) and EM profile (**Figure 9C,D**). We termed one class AF-neuromodulatory (AF-Nm, n=14). In this
483 class, on the 468 boutons reconstructed we annotated 1460 postsynaptic sites and only 3 presynaptic sites,
484 with a median of 3.2 postsynaptic site per bouton. Each bouton formed a rosette structure of axo-axonal
485 synapses where several SAMs made adjacent synapses onto one AF bouton (**Figure 9C**). The postsynaptic
486 sites were filled mostly with large dense core vesicles (60-80 nm), suggesting a neuromodulatory nature.
487 The synaptic inputs of the SAMs into the AF-Nm boutons may suggest SAMs-induced local extrasynaptic
488 release of neuromodulator (see Discussion). The AFs seem morphologically equivalent to the serotonergic
489 processes ascending into the cell cortex found in immunohistological studies (Shomrat et al. 2010; Shigeno
490 and Ragsdale 2015) and also to tyrosine hydroxylase (catecholaminergic) labeled processes (Stern-Mentch
491 et al., 2022).

492 In contrast, the second class of AF, the AF-mix (N=18), were more diverse with boutons filled with vesicles
493 of varying shape and size (30-90 nm; N=519), including small dark core vesicles, flat clear core vesicles
494 and larger vesicles. Unlike the AF-Nm, the AF-mix were both presynaptic (median of 0.2 presynaptic
495 sites/bouton) and postsynaptic (median of 0.6 postsynaptic sites/bouton) and occasionally displayed
496 reciprocal contact with a SAM (**Figure 9D**). The diverse nature of the synaptic vesicles in the two subtypes
497 suggests that they convey different neuromodulatory signals and the reciprocal connection with the SAMs
498 suggest their involvement in SAM -induced local release of neuromodulators.

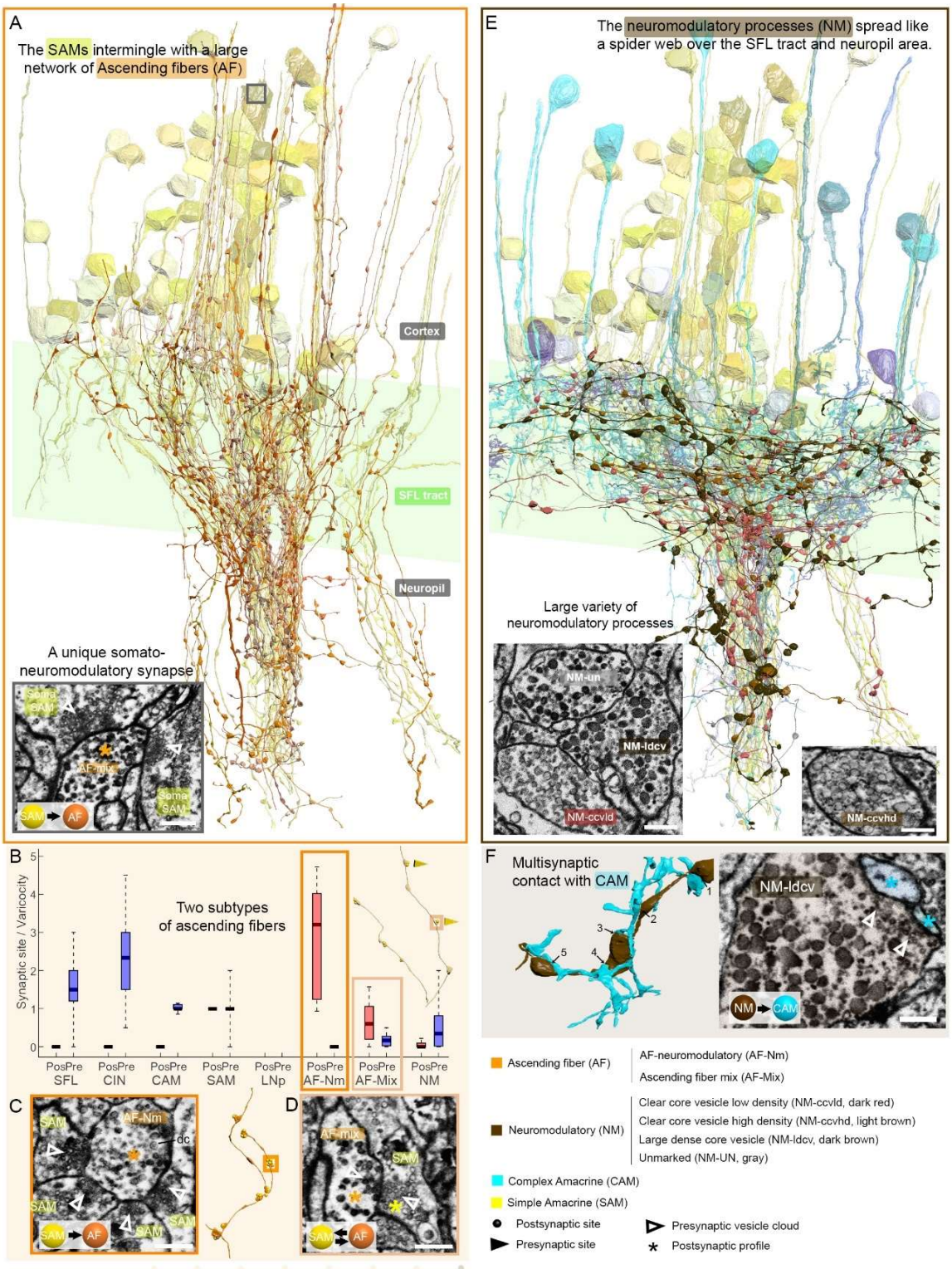

Figure 9. Overlay of two modulatory systems, the ascending fibers (AFs) and widespread neuromodulatory fibers (NMs). (A) 3D reconstruction of a large network of AFs (orange) intermingling with a SAM neuritic bundle (yellow). The AFs showed varicosities along their length filled with large

503 vesicles and were mainly postsynaptic to the SAMs (C,D) A somatic synaptic input from SAM to AF was
504 occasionally observed (lower left inset). (B) The distribution of the number of pre- and postsynaptic sites
505 per varicosity (blue and red, respectively) revealed two types of AF processes shown in C and D. (C) The
506 AF-Nm type (orange) were exclusively unidirectional synapses forming a rosette-like structure where 2-5
507 SAMs made adjacent synapses onto one AF-Nm postsynaptic varicosity (asterisk). (D) The AF-mix (light
508 orange) were more diverse. Their boutons were filled with vesicles of various shapes and sizes, ranging
509 from small dark core vesicles to flat clear core vesicles. Unlike the AF-Nm, they could be bidirectional,
510 both pre- and postsynaptic (triangles and puncta, respectively) and occasionally displayed reciprocal contact
511 with a SAM as shown in the EM. (E) 3D reconstruction of the widespread NM fibers color coded by subtype
512 and superimposed on populations of SAMs (yellow) and CAMs (blue). At least 3 distinct subtypes were
513 distinguishable based on vesicle sizes (EM insets: clear core low density, clear core high density, dense
514 core). (F) 3D reconstruction of NM-to-CAM synapses. The NM made multisynaptic contacts. The right
515 inset shows a representative EM of a neuromodulatory synapse. Scale bar EM sections, 500 nm. See **Figure**
516 **9–figure supplement 1**
517

518 **The ubiquitous NM processes appear to be involved in global neuromodulatory signaling via**
519 **extrasynaptic transmission**

520 A large variety of processes displayed the largest dense vesicles (60-200nm), which appear similar to
521 vesicles thought to be neuromodulatory in other invertebrates (Messenger 1996; Witvliet et al. 2021). The
522 processes were widespread within the neuropil and the SFL tract and their lack of specific orientation made
523 it impossible to assume their origin (**Figure 9E**). At least 3 distinct profiles were clearly distinguishable by
524 vesicle size and appearance, showing either a low density of clear core vesicles, a high density of clear core
525 vesicles or very large dense core vesicles. The boutons of each process contained only one type of vesicle,
526 which were also present within the fiber. Reconstructions of NM processes (N=88) showed that most of the
527 boutons had neither inputs nor outputs (464/632), suggesting that they were neuromodulatory afferents
528 which exert their effects through extrasynaptic volume transmission. Yet, these cells occasionally synapsed
529 with a variety of postsynaptic partners including CAMs, SAMs AFs, NMs themselves, and LNs (**Figure 2**
530 **and Figure 2 - figure supplement 1**). Multisynaptic contacts were occasionally observed, for instance,
531 with CAMs (**Figure 9F**), but the density of synaptic sites per bouton was rather low, 52 presynaptic sites
532 and 250 postsynaptic sites on 632 boutons. Accordingly, NM processes may be involved primarily in
533 extrasynaptic transmission and thus may convey a global modulatory signal transmitted though action
534 potentials propagating along them.

535

536 **DISCUSSION**

537 The novel connectivity and anatomical features discovered here profoundly advance our understanding of
538 the functional organization of the learning and memory circuits in the vertical lobe (VL) of *Octopus*
539 *vulgaris*. The EM volume reconstruction revealed several novel features that, on one hand, show the VL is
540 composed of several more components than previously thought. On the other hand, these novel cell types
541 and their connectivity help us understand the functional organization of the VL as a learning and memory
542 acquisition network.

543 **The 25 million amacrine interneurons in the VL input layer are not a homogeneous group**

544 The first striking finding was that 89% of the 25 million AM interneurons (**Figure 4**) send a simple non-
545 bifurcating neurite into the neuropil and were therefore termed simple AMs (SAMs; **Figure 6A**). The SAMs
546 are highly input specific as each received *en passant* input from only a single SFL axon via large presynaptic
547 boutons (LB) (**Figure 3A, Figure 5 and Figure 6A1**). If the pattern of one-to-one innervation is maintained
548 throughout the whole SFL tract and if, as generally believed and as found here, the SFL axons bifurcate
549 very rarely, then every SFL neuron is represented by only around 12 ± 3.46 SAMs ($22x10^6$ SAMs / $1.8x10^6$
550 SFLs). Moreover, the LBs seem to be sparsely distributed along the SFL axon (1.03 ± 0.73 LBs per 100
551 µm; see Results), suggesting that each SFL neuron is represented in the SAMs in a highly sparse and non-
552 overlapping fashion.

553 This extremely low and random topographical expansion of SFL inputs to SAMs is unique for input
554 circuitry. In *Drosophila* mushroom bodies, for example, the expansion ratio is multiplied by a factor of
555 about 6 as six projecting neurons converge onto each Kenyon cell (Li et al. 2020) and in locust the expansion
556 ratio is 400 (Jortner et al. 2007). The unique low expansion of information in the VL is achieved by the
557 formation of a huge number of SAMs, 3-4 orders of magnitude more than the number of the homologous
558 Kenyon cells in the insect mushroom bodies. This mode of expansion may be related to the organization of
559 the octopus visual system where each SFL axon carries visual information that has been highly processed
560 by the $120x10^6$ neurons of the two optic lobes and then possibly further classified into lower dimensional
561 visual features in the only $1.8x10^6$ cells in the SFL (Young 1971). This unusual expansion pattern resembles
562 the $50x10^{12}$ granular cells in the human and mice cerebellum - each receiving only 4-6 inputs from the
563 mossy fibers at the expansion ratio of 1-to-200 (D'Angelo 2013; Kawato et al. 2021). An additional striking
564 similarity is that these unique synaptic connections in the cerebellum undergo activity-dependent
565 presynaptic LTP; (Mapelli and D'Angelo 2007) like the SFL-to-SAM synapse in the octopus VL.

566 Our second novel discovery is that the AMs included a small group of a new class of AM neuron, only
567 1.6% of the AMs in the VL cortex (**Figure 4**). These neurons showed a bifurcating dendritic structure and

568 were therefore termed complex AMs (CAMs, **Figure 6B**). The primary neurite segments of the SAMs and
569 CAMs travel together in the AM bundles within the VL cortex, but the non-bifurcating SAM neuritic trunks
570 cross the SFL tract to pass into the inner neuropil, while the CAM neurites bifurcate substantially within
571 the SFL tract (**Figure 2 and Figure 6B**). The CAMs receive inputs *en passant* from multiple SFL axons
572 either directly or indirectly via a serial connection from the SAMs (**Figure 5 and Figure 6B**). Thus, while
573 each SAM represents a single SFL neuron, the CAMs integrate information from dozens to hundreds of
574 SFL neurons together with multiple inputs from nearby SAMs. In addition, as discussed below, the CAMs
575 receive inputs from afferents from a yet unidentified origin, which exclusively innervate CAMs (CIN,
576 **Figure 6B3 and Figure 8**).

577 **The SFL axons innervate the SAMs and CAMs via different classes of presynaptic boutons**

578 SAMs and CAMs are innervated by SFL axons via small (SFL SB) or extremely large boutons (SFL LB –
579 **Figure 3**). The LBs are always associated with at least one SAM palm and may additionally innervate a
580 CAM twig within a dyadic or triadic arrangement (**Figure 5**). By contrast, SBs are always associated with
581 a single postsynaptic CAM compartment (**Figure 3**). This suggests that the two different types of SFL axon
582 terminal are functionally specialized. Such functional segregation is also seen in the hippocampal mossy
583 fiber connections where small boutons target GABAergic interneurons, whereas large boutons contact CA3
584 pyramidal cells and hilar mossy cells (Acsády et al. 1998). The latter large synapse shares several synaptic
585 features with the octopus VL synapses (Hochner et al. 2003) – NMDA-independent, presynaptically
586 expressed LTP and an extremely large range of presynaptic short-and long-term synaptic gain modulations
587 (Nicoll and Schmitz 2005; Henze et al. 2000; Hainmueller and Bartos 2020; Restivo et al. 2015). The large
588 synaptic boutons here, like the mossy fiber terminals, may provide an increased dynamical range of synaptic
589 gain control needed for certain forms of plasticity involving presynaptic modulation of transmitter release
590 (Orlando et al. 2021; Hainmueller and Bartos 2020; Restivo et al. 2015).

591 **The single SFL synaptic input into the SAM may serve as a gain control site of the stimulus-specific**
592 **input to the VL**

593 Each SAM receives synaptic input from only a single SFL neuron, raising the question of the role of such
594 apparently non-integrating interneurons. Physiological results indicate that the glutamatergic SFL-AM
595 synapse is the site of activity-dependent LTP in the VL (Hochner et al. 2003; Shomrat et al. 2011; Turchetti-
596 Maia et al. 2018). The large volume of the SFL-LB relative to that of the SFL-SB found here (on average
597 6-fold larger) suggests that the recorded synaptic field potential (fPSP) mainly reflects the synaptic input
598 from the SFL LB to the SAMs. The morphological dimensions of the SAMs revealed here (*e.g.,* a 166µm
599 long 0.5µm diameter neuritic trunk emerging from a 7µm diameter cell body) together with previous
600 electrophysiological measurements (>1GΩ input resistance measured at the cell body), suggest that the

601 inexcitable SAMs (Hochner et al. 2003, 2006)are electrotonically compact (estimated length constant λ >
602 147 μm) (Hochner and Spira 1987), so that the glutaminergic excitatory postsynaptic potential from the
603 SFL LB input site is likely sufficient to activate voltage-dependent transmitter release down the SAM
604 neurite without needing a propagating action potential. These inexcitable properties, which differ drastically
605 from the excitable properties of the insects Kenyon cells (e.g. Demmer and Kloppenburg 2009), explain
606 nicely the linear input/output relationship of the SAMs (Shomrat et al. 2011). Since the activity-dependent
607 changes at the SFL-SAM synapse involve pre- and postsynaptic mechanisms (see below), we suggest that,
608 rather than being simple relay interneurons, the SAMs provide a synaptic "gain-control relay" of the SFL-
609 LB input into the CAMs and LNs.

610 **How can specificity and associativity be achieved within these one-to-one SFL-to-SAM connections?**

611 *Specificity* and *associativity* are essential properties for all associative learning networks (Kandel et al.,
612 2012; Malenka 2003). To understand how they are achieved within the unique wiring of the VL it is
613 important to recall that LTP expression in the VL involves presynaptic facilitation of transmitter release
614 from the SFL boutons. This was suggested to be mediated by an activity-dependent persistence elevation
615 of NO concentration in the vicinity of the SFL-SAM connection. NO alone cannot induce LTP. Only the
616 association of strong activation of an SFL- SAM synapse switches ON the NO-dependent NOS activation,
617 leading to long-term LTP *maintenance* (Turchetti-Maia et al. 2018). The good correspondence of the
618 SAMs' morphological characteristics with AM-specific labeling by NADPH-diaphorase and cChAT
619 (choline acetyl transferase) suggests that NOS activity is strongly expressed along the entire length of the
620 cholinergic SAMs (Stern-Mentch et al. 2022). Accordingly, NO, which can readily diffuse short distances
621 through cell membranes (Agnati et al., 1995; Garthwaite, 2016, 2020; Turchetti-Maia et al., 2017, 2018)
622 and which is generated in the SAMs following LTP induction, diffuses retrogradely from the SAM palm
623 into the presynaptic SFL LB mediating the NO-dependent presynaptic *expression* of LTP. The
624 characteristic morphological arrangement described here with the SAM palm partly wrapping the SFL LB,
625 ensures synaptic specificity as the steep NO concertation gradient will affect only these closely attached
626 presynaptic varicosities (Hall and Garthwaite 2009). The SFL- SAM synapses are organized in a compact
627 synaptic glomerulus that may facilitate the diffusion of NO within a triadic synaptic organization including
628 the CAMs. This suggests that NO diffusing from a single postsynaptic SAM palm also modulates the SFL
629 SB input into the CAMs.

630 What are the possible mechanisms of LTP *associativity*? The persistence elevation of NO concentration in
631 the VL is maintained, at least in about half of SFL-SAM synapses, through a molecular switch consisting
632 of a positive feedback loop of NO-dependent reactivation of NOS (Turchetti-Maia et al. 2018). This
633 "molecular switch" provides a tentative molecular model for associativity, whereby volume-type

transmission of NO (Garthwaite 2016) between adjacent activated SAMs may mutually facilitate associative switching ON of NOS in these simultaneously activated SAMs. Our results highlighted that many SAM neurites converging within the neuropil to form compact bundles of thin intermingling processes travelling together (**Figure 7A**). Such spatially closed arrangements of thin neurites (e.g., **Figure 7A, C**), which express intense NOS activity (see Turchetti-Maia et al., 2018, Stern-Mentch et al 2022), can favor mutual NO effects among adjacent SAM neurites.

The CAMs as a putative feedforward inhibitory network balancing the parallel SAM feedforward excitatory network.

The newly discovered CAMs comprise only 1.6% of the 25 million small interneurons in the VL cortex. An inhibitory nature of CAMs is supported by GABA labeling of putative CAM dendritic processes at the level of the SFL tract and in varicosities in the neuropil (Stern-Mentch et al. 2022). Also, inhibitory CAMs would explain the IPSPs or EPSP followed with short delay by an IPSP recorded in some of the LNs in response to SFL tract stimulation (**Figure 7 - figure supplement 1**).

Although the CAMs show morphological diversity (**Figure 6- figure supplement 2 and 3**), they share similar connectivity, integrating multiple inputs from the SFLs, SAMs and CAM-specific inputs (CIN) in their bifurcating dendrites (**Figure 6B**). The CAMs innervate the LN dendritic processes only sparsely, unlike the dense LN innervation by the SAMs (**Figure 7B and 7D**). This innervation pattern suggests that the LNs integrate stimulus-specific excitatory inputs from many SAMs, while the CAMs, which integrate ubiquitous and nonselective inputs, are optimally located for inhibitory balancing the overall SAM excitatory inputs. Yet, the LNp are innervated by only a few CAMs, suggesting that the CAMs inhibitory inputs are activated simultaneously over a large LN dendritic area causing widespread postsynaptic inhibition of the LNp.

If the CAMs are indeed inhibitory interneurons, then our results strongly suggest the VL network is organized into two interconnected parallel feedforward networks, in which the SFL axons conveying sensory inputs 'fan-out' onto SAMs (in ~1/12 ratio) and 'fan-in' (~4/1) onto the CAMs. Both the SAMs and CAMs feedforward onto the LNs in the VL readout layer (schematically shown in **Figure 10A**). This type of organization may sharpen the stimulus specific SAM inputs to the LNs by subtracting the global or background activity monitored by the inhibitory CAMs. This type of organization may highlight a universal inhibitory balancing organization in networks with different functions. A similar organization is found in cortical circuits representing sparse, odor-specific, activity where the sparse activity is generated through summing unbalanced widespread and broadly tuned inhibition with odor-specific excitation (Poo and Isaacson 2009). In the octopus VL, such sharpening mechanism may ensure recognition of learned visual scenarios even under variable light intensities. Theoretical studies have demonstrated the importance of

667 implementing feedforward inhibition parallel to the feedforward excitation to balance the stable
668 propagation of an activity wave (Litvak et al., 2003). Feedforward inhibition also appears important for
669 balancing networks' input/output relationships to avoid attraction of network activity into either up or down
670 states (Ferrante et al., 2009). Finally, long-term balancing inhibition is believed to be important in ensuring
671 network homeostasis especially in networks involved in learning and memory, like the hippocampus, where
672 activity balances may be perturbated by long-term activity-dependent plasticity (Turrigiano and Nelson
673 2004).

674 **Three candidates for conveying modulatory signals.**

675 Learning and memory networks are usually supervised by neuromodulation. Early anatomical studies by
676 Young and colleagues proposed several candidates, and our study has refined Young's broad classification
677 of fibers ascending to the VL. We have described 3 distinct classes of putative extrinsic processes:
678 neuromodulatory fibers (NM), ascending fibers (AF) and CAM-specific input fibers (CIN). These could
679 play a role in conveying information on whether the current environment is punitive or rewarding,
680 reinforcing, or suppressing associative learning.

681 The rich and widely distributed NMs intermingle with the fast transmitter feedforward network
682 (schematized in **Figure 10B**). The fibers form a mesh in the neuropil and may be associated with regulation
683 of overall VL activity. Their exceptionally large boutons, frequently lacking the typical release sites, are
684 filled with a variety of large dense-core vesicles of the type usually storing and releasing neuropeptides and
685 non-classical neurotransmitters (Zhu et al. 1986; Leng and Ludwig 2008; van den Pol 2012; Witvliet et al.
686 2020). A variety of neuropeptides and hormones have been identified in the *Octopus vulgaris* VL -
687 serotonin, dopamine, octopamine, FMRFamide-related peptides, vasopressin, oxytocin, octopressin, Y-
688 peptide and more (Shomrat et al. 2010; Shigeno and Ragsdale 2015; Winters et al. 2020; Stern-Mentch et
689 al. 2022). Tyrosine hydroxylase (TH) - labeled processes show a wide distribution in the VL neuropil
690 similar to that of the NM processes, suggestive of a neuromodulatory catecholamine innervation (Stern-
691 Mentch et al. 2022).

692 As schematized in **Figure 10B**, the AF fibers form close associations with the SAMs (**Figure 9A**), while
693 the CIN fibers appear to exclusively innervate the CAMs (**Figure 8, schematized in Figure 10A**). The AF
694 boutons form a rosette-like structure in which several SAMs make adjacent synapses onto one AF bouton,
695 mostly filled with dense-core vesicles. Such a connectivity motif between neurons and neuromodulatory
696 processes suggests that co-activated SAMs may activate an AF bouton that, in turn, releases a
697 neuromodulator. This mechanism can function locally, especially if the AF processes are inexcitable. Local
698 release of the neuromodulator can heterosynaptically induce synaptic plasticity, similar to the well-known
699 heterosynaptic serotonin-dependent synaptic plasticity, particularly in the gastropods mollusc *Aplysia*

700 (Bailey et al. 2000; Kandel et al. 2014). The reciprocal SAM AF connection in the VL network is a plausible
701 synaptic motif that may suggest a "self" LTP-induction mechanism as shown schematically in Figure 10B.

702 The feasibility of such a mechanism is hinted at by 5-HT causing both short-term synaptic facilitation of
703 the input to the AMs and reinforcing LTP induction (Shomrat et al. 2010). Dopamine and octopamine also
704 affect synaptic physiology but, in contrast to 5-HT, they suppress the transition to LTP maintenance
705 (unpublished results). Immunohistochemical studies have also revealed a rich distribution of serotonin-
706 (Shomrat et al. 2010; Shigeno and Ragsdale 2015) and catecholaminergic-rich fibers (Stern-Mentch et al.
707 2022) that resembles the AF distribution described here, suggesting possible AF involvement in modulation
708 of the activity-dependent LTP. While Shomrat et al. (2010) found serotonergic immunoreactive cell bodies
709 outside the VL and in the subvertical lobe, Stern-Mentch et al. (2022) described a group of TH-labeled cell
710 bodies organized as a "deep nucleus" at the border between the SFL and VL. This suggests that, while
711 incoming serotonergic innervation may provide supervision signals, like reward and punishment (Turchetti-
712 Maia et al. 2017), a dopaminergic system may be involved in the regulation of the internal state of the SFL-
713 VL system.

714 The exclusive innervation of the very small group of CAMs by a distinct group of processes (CIN) must be
715 functionally significant (schematically shown in **Figure 10A**). The CIN processes resemble fibers that
716 Young speculated were ascending fibers carrying "pain signals" from the arms and mantle (Gray, 1970;
717 Gray and Young, 1964). Unlike the NMs and AFs that barely display any presynaptic profiles, the CIN
718 outputs to the CAMs have the typical morphological features of fast transmitter synapses (**Figure 8**). The
719 presynaptic features are similar to vertebrate presynaptic terminals, with small electron-dense synaptic
720 vesicles, which are occasionally associated with inhibitory synapses (McDonald et al. 2002; Kasthuri et al.
721 2015). We therefore speculate that, in addition to feedforward excitation from the SFLs and SAMs, the
722 CAMs integrate inhibitory inputs from the CIN. The CINs may provide negative feedback adjusting the
723 level of LNs output to that of its targets, such as the subvertical lobe to where the LNs axons project and
724 which Young described as the origin of the "pain fibers." In the framework of the VL model (Shomrat et
725 al. 2015b; Turchetti-Maia et al. 2017), in which the GABAergic LN output (Stern-Mentch et al. 2022)
726 inhibits the octopus' tendency to attack, the CIN inhibitory input onto the CAMs would increase the LN
727 output, resulting in suppression of the attack behavior. We believe this is what occurs when training
728 octopuses on a passive avoidance task (Shomrat et al. 2008).

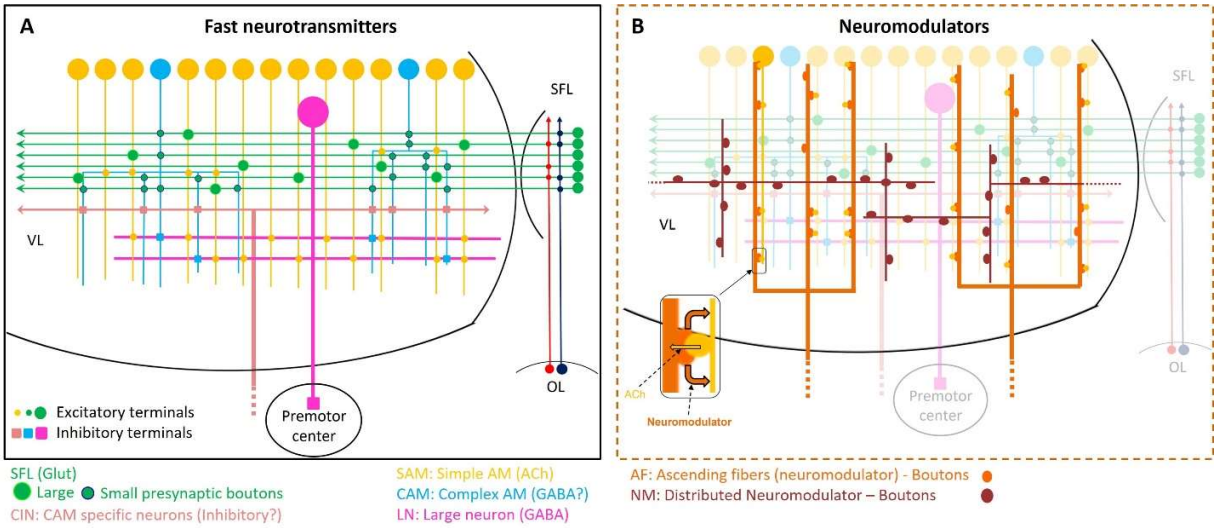

Figure 10. Schematic representation of the currently known circuit architecture of the VL. (A) Fast transmitter connectivity. The parallel SFL axonal tract (green) conveys classified sensory information via *en passant* glutamatergic (glut) synapses to a large group of SAMs (yellow) and a very small group of CAMs (cyan). Each SAM has one palm on its neurite innervated by a single large SFL bouton (SFL LB). This connection is endowed with short- and long-term plasticity. The CAMs integrate ongoing activity through multiple inputs from the SFL, SAMs and CINs (light pink). The SAMs and CAMs converge onto the LN processes (LNp, magenta) forming two parallel and interconnected feedforward networks (shown in **Figure 11**). SAM output to the LNs is excitatory cholinergic (ACh). The CAMs inputs to the LN may be inhibitory GABAergic (see text). (B) The two widespread networks of modulatory inputs into the fast transmission circuit (shown in A). The ascending AF processes (orange) make reciprocal connections with the SAM neurites, possibly inducing local release of neuromodulator (likely serotonin). The NMs (brown) spread throughout the neuropil. Physiological and immunohistochemical studies indicate that AFs and NMs release neuromodulators such as serotonin and octopamine and dopamine that likely play a role in reinforcing/suppressing the LTP at the SFL-to-SAM synapse.

Many SAMs together with a few CAMs appear to be organized in a canonical "association module"

Our reconstructions highlighted that ensembles of closely intermingled groups of SAM and CAM neurites form a *quasi*-columnar structural unit (**Figures 7A,7C,9A,9E, Figure - figure supplement 1**). As suggested above, this group of closely packed thin neurites likely functions as an "association module". The neurons in each module may respond to a combinatorial ensemble of sensory features from the SFL, as schematically represented in **Figure 11 inset**. Such combinatorial coding is a common feature in association networks such as the insect and mammalian olfactory systems (Malnic et al. 1999; Lledo et al. 2005; Galizia and Szyszka 2008; Turner et al. 2008; Gruntman and Turner 2013; Kurian et al. 2021). However, the one-to-one SFL-to-SAM connections suggest that each SFL neuron is represented in probably less than 12 ± 3.6 SD SAMs, most of them in different modules spread randomly over the VL cortex (**Figure 11**). This suggests that each of VL association module associates many (i.e., several hundreds of SMAs) random combinations of visual features that are represented in the 1.8 million SFL neurons. As the number

of association modules in the VL is very large (tens of thousands) it may enable the VL to "learn" the huge amount of data associated with storing the visual environment. In principle the “association module” is equivalent to that of a single interneuron in the input layer of a classical “fan-out fan-in” classification network as proposed in Shomrat et al., (2011). However, the processing power provided by the association module is computationally more elaborated than a single neuron can provide. It is tempting to speculate that what is achieved in other systems by a single complex neuron is achieved in the octopus by the construction of a microcircuitry composed of many neurons with simple properties (e.g., a linear input/output relationship).

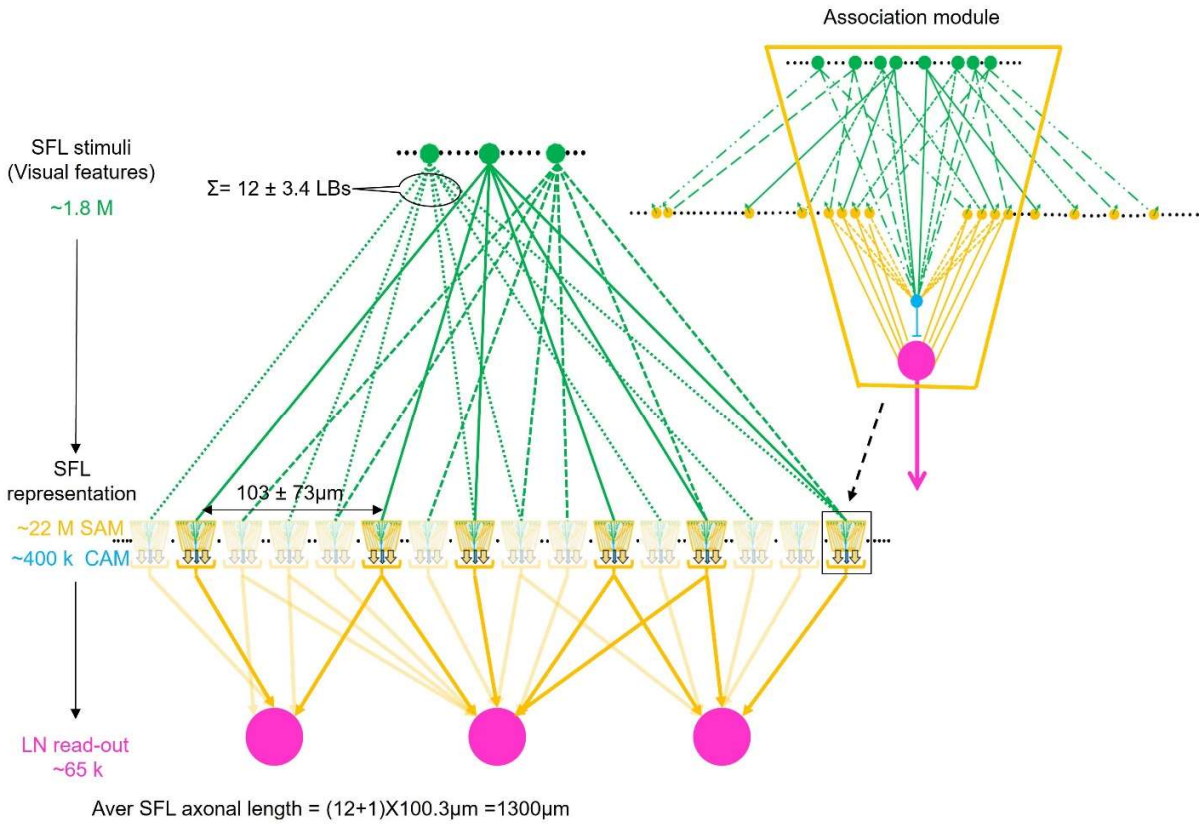

Figure 11. Schema of combinatorial coding in possible association modules array. ***Inset:*** The SAMs and CAMs appear to be organized in columnar structures that integrate and feedforward “sharpened” stimulus-specific inputs into the LNs. A specific stimulus (e.g., a visual feature) is fed forward via the SAMs while the CAMs integrate these and the SAM inputs together and feed a general balancing inhibitory input forward to the LNs. As the input to the SAMs is endowed with LTP, we suggest that this microcircuit unit is a canonical “association module” of the VL. ***The main scheme*** shows how an array of association modules that integrates a very sparse and randomly distribution of the SFL single input to the SAMs (1.0 3 ± 0.73 LBs per 100μm). Each association module contains likely several hundred SAMs and relatively only few CAMs (1.8%) suggesting that each module associates a variable combinatorial association of multiple SFL features. Note that computationally an association module replaces a single AM in the input layer of the originally assumed fan-out fan-in classification/association network (Shomrat et al 2011).

In summary, while earlier reports (Gray and Young 1964; Gray 1970; Young 1971) suggested that the VL is organized in a simple fan-out fan-in feedforward architecture much like an associative "perceptron" network (Shomrat et al. 2011), our study has revealed that its organization is more complex. Indeed, the VL circuitry is characterized by two parallel and interconnected feedforward networks that are assembled in what appear to be association modules, in which the SFL axons that convey processed sensory inputs fan-out into many SAMs and fan-in into a low number of CAMs. Both SAMs and CAMs feed the excitatory and inhibitory inputs, respectively, forward into the LN output layer.

AKNOWLEDGMENTS

This work was supported by Human Frontier Science Program (HFSP) grant no. RGP0042/2019-102, Israel Science Foundation (ISF) grant no. 1928/15, National Institutes of Health (NIH) grant no. U19 NS104653, U24 NS109102-01, NIH 1U01NS108637.We would like to thank Prof. Jenny Kien for editing the manuscript.

Author contributions Sample preparation, F.B., Y.M., X.L.; sectioning, R.L.S.; imaging, F.B and R.L.S.; alignment, A.P. and Y. W.; manual segmentation, F.B, F.Y., X.L. and A.S.; machine learning-aided segmentation tool development, Y.M. and E.C.P.; Figures, F.B; Videos, Y.M and D.R.B.; statistical analyses., F.B. and Y.M..; 3D renderings, F.B. and D.R.B.; electrophysiological data., T.S. and B.H.; writing, F.B, Y.M and B.H.; review, D.R.B.; funding acquisition, J.W.L and B.H.; guidance, J.W.L

Declaration of interests

The authors declare no competing interests.

REFERENCES

Acsády L, Kamondi A, Sík A, et al (1998) GABAergic cells are the major postsynaptic targets of mossy fibers in the rat hippocampus. J Neurosci 18:3386–3403

Agnati LF, Zoli M, Strömberg I, Fuxe K (1995) Intercellular communication in the brain: Wiring versus volume transmission. Neuroscience 69:711–726. https://doi.org/10.1016/0306-4522(95)00308-6

Aso Y, Hattori D, Yu Y, et al (2014) The neuronal architecture of the mushroom body provides a logic for associative learning. eLife 3:e04577. https://doi.org/10.7554/eLife.04577

Bailey CH, Giustetto M, Huang Y-Y, et al (2000) Is Heterosynaptic modulation essential for stabilizing hebbian plasiticity and memory. Nat Rev Neurosci 1:11–20. https://doi.org/10.1038/35036191

Barth W, Mutzel P, Jünger M (2004) Simple and Efficient Bilayer Cross Counting. JGAA 8:179–194. https://doi.org/10.7155/jgaa.00088

Bentley B, Branicky R, Barnes CL, et al (2016) The Multilayer Connectome of Caenorhabditis elegans. PLOS Computational Biology 12:e1005283. https://doi.org/10.1371/journal.pcbi.1005283

Berger DR, Seung HS, Lichtman JW (2018) VAST (Volume Annotation and Segmentation Tool): Efficient Manual and Semi-Automatic Labeling of Large 3D Image Stacks. Front Neural Circuits 12:. https://doi.org/10.3389/fncir.2018.00088

Boycott BB, Young JZ (1955) A Memory System in Octopus vulgaris Lamarck. Proceedings of the Royal Society of London B: Biological Sciences 143:449–480. https://doi.org/10.1098/rspb.1955.0024

D'Angelo E (2013) Cerebellar Granule Cell. In: Manto M, Schmahmann JD, Rossi F, et al. (eds) Handbook of the Cerebellum and Cerebellar Disorders. Springer Netherlands, Dordrecht, pp 765–791

Demmer H, Kloppenburg P (2009) Intrinsic membrane properties and inhibitory synaptic input of kenyon cells as mechanisms for sparse coding? J Neurophysiol 102:1538–1550. https://doi.org/10.1152/jn.00183.2009

Dowling JE, Boycott BB, Wells GP (1966) Organization of the primate retina: electron microscopy. Proceedings of the Royal Society of London Series B Biological Sciences 166:80–111. https://doi.org/10.1098/rspb.1966.0086

Feinstein N, Nesher N, Hochner B (2011) Functional morphology of the neuromuscular system of the Octopus vulgaris arm. Vie Milieu 11

Ferrante M, Migliore M, Ascoli GA (2009) Feed-forward inhibition as a buffer of the neuronal input-output relation. PNAS 106:18004–18009. https://doi.org/10.1073/pnas.0904784106

Fiorito G, Chichery R (1995) Lesions of the vertical lobe impair visual discrimination learning by observation in< i> Octopus vulgaris</i>. Neuroscience letters 192:117–120

838 Fischler MA, Bolles RC (1981) Random sample consensus: a paradigm for model fitting with
839 applications to image analysis and automated cartography. Commun ACM 24:381–395.
840 https://doi.org/10.1145/358669.358692

841 Fruchterman TMJ, Reingold EM (1991) Graph drawing by force-directed placement. Software:
842 Practice and Experience 21:1129–1164. https://doi.org/10.1002/spe.4380211102

843 Galizia CG, Szyszka P (2008) Olfactory coding in the insect brain: molecular receptive ranges,
844 spatial and temporal coding. Entomologia Experimentalis et Applicata 128:81–92.
845 https://doi.org/10.1111/j.1570-7458.2007.00661.x

846 Garthwaite J (2016) From synaptically localized to volume transmission by nitric oxide. The
847 Journal of Physiology 594:9–18. https://doi.org/10.1113/JP270297

848 Gray EG (1970) The Fine Structure of the Vertical Lobe of Octopus Brain. Philosophical
849 Transactions of the Royal Society B: Biological Sciences 258:379–394.
850 https://doi.org/10.1098/rstb.1970.0040

851 Gray EG, Young JZ (1964) Electron microscopy of synaptic structure of Octopus brain. J Cell
852 Biol 21:87–103

853 Gruntman E, Turner GC (2013) Integration of the olfactory code across dendritic claws of single
854 mushroom body neurons. Nat Neurosci 16:1821–1829. https://doi.org/10.1038/nn.3547

855 Hanlon RT, Messenger JB (2018) Cephalopod Behaviour. Cambridge University Press

856 Hayworth KJ, Morgan JL, Schalek R, et al (2014) Imaging ATUM ultrathin section libraries with
857 WaferMapper: a multi-scale approach to EM reconstruction of neural circuits. Frontiers in
858 Neural Circuits 8:. https://doi.org/10.3389/fncir.2014.00068

859 Hochner B (2010) Functional and comparative assessments of the octopus learning and
860 memory system. Front Biosci (Schol Ed) 2:764–771

861 Hochner B (2012) An Embodied View of Octopus Neurobiology. Current Biology 22:R887–
862 R892. https://doi.org/10.1016/j.cub.2012.09.001

863 Hochner B (2013) How nervous systems evolve in relation to their embodiment: what we can
864 learn from octopuses and other molluscs. Brain Behav Evol 82:19–30.
865 https://doi.org/10.1159/000353419

866 Hochner B, Brown ER, Langella M, et al (2003) A Learning and Memory Area in the Octopus
867 Brain Manifests a Vertebrate-Like Long-Term Potentiation. Journal of Neurophysiology
868 90:3547–3554. https://doi.org/10.1152/jn.00645.2003

869 Hochner B, Glanzman DL (2016) Evolution of highly diverse forms of behavior in molluscs. Curr
870 Biol 26:R965–R971. https://doi.org/10.1016/j.cub.2016.08.047

871 Hochner B, Shomrat T, Fiorito G (2006) The octopus: a model for a comparative analysis of the
872 evolution of learning and memory mechanisms. Biol Bull 210:308–317.
873 https://doi.org/10.2307/4134567

874 Hochner B, Spira ME (1987) Preservation of motoneuron electrotonic characteristics during
875 postembryonic growth. J Neurosci 7:261–270

876 Holm S (1979) A simple sequentially rejective multiple test procedure. Scandinavian Journal of
877 Statistics 6:65–70

878 Jortner RA, Farivar SS, Laurent G (2007) A Simple Connectivity Scheme for Sparse Coding in
879 an Olfactory System. J Neurosci 27:1659–1669.
880 https://doi.org/10.1523/JNEUROSCI.4171-06.2007

881 Kandel ER, Dudai Y, Mayford MR (2014) The Molecular and Systems Biology of Memory. Cell
882 157:163–186. https://doi.org/10.1016/j.cell.2014.03.001

883 Kasthuri N, Hayworth KJ, Berger DR, et al (2015) Saturated Reconstruction of a Volume of
884 Neocortex. Cell 162:648–661. https://doi.org/10.1016/j.cell.2015.06.054

885 Kawato M, Ohmae S, Hoang H, Sanger T (2021) 50 Years Since the Marr, Ito, and Albus
886 Models of the Cerebellum. Neuroscience 462:151–174.
887 https://doi.org/10.1016/j.neuroscience.2020.06.019

888 Kier WM (1996) Muscle development in squid: Ultrastructural differentiation of a specialized
889 muscle fiber type. J Morphol 229:271–288. https://doi.org/10.1002/(SICI)1097-
890 4687(199609)229:3<271::AID-JMOR3>3.0.CO;2-1

891 Koren Y (2005) Drawing graphs by eigenvectors: theory and practice. Computers &
892 Mathematics with Applications 49:1867–1888.
893 https://doi.org/10.1016/j.camwa.2004.08.015

894 Kurian SM, Naressi RG, Manoel D, et al (2021) Odor coding in the mammalian olfactory
895 epithelium. Cell Tissue Res 383:445–456. https://doi.org/10.1007/s00441-020-03327-1

896 Lee K, Zung J, Li P, et al (2017) Superhuman Accuracy on the SNEMI3D Connectomics
897 Challenge

898 Lee W-CA, Bonin V, Reed M, et al (2016) Anatomy and function of an excitatory network in the
899 visual cortex. Nature 532:370–374. https://doi.org/10.1038/nature17192

900 Leiss F, Groh C, Butcher NJ, et al (2009) Synaptic organization in the adult Drosophila
901 mushroom body calyx. Journal of Comparative Neurology 517:808–824.
902 https://doi.org/10.1002/cne.22184

903 Leng G, Ludwig M (2008) Neurotransmitters and peptides: whispered secrets and public
904 announcements. J Physiol 586:5625–5632. https://doi.org/10.1113/jphysiol.2008.159103

905 Li F, Lindsey JW, Marin EC, et al (2020) The connectome of the adult Drosophila mushroom
906 body provides insights into function. eLife 9:e62576. https://doi.org/10.7554/eLife.62576

907 Litvak V, Sompolinsky H, Segev I, Abeles M (2003) On the Transmission of Rate Code in Long
908 Feedforward Networks with Excitatory–Inhibitory Balance. J Neurosci 23:3006–3015.
909 https://doi.org/10.1523/JNEUROSCI.23-07-03006.2003

Lledo P-M, Gheusi G, Vincent J-D (2005) Information Processing in the Mammalian Olfactory System. Physiological Reviews 85:281–317. https://doi.org/10.1152/physrev.00008.2004

Lowe DG (1999) Object recognition from local scale-invariant features. In: Proceedings of the Seventh IEEE International Conference on Computer Vision. IEEE, Kerkyra, Greece, pp 1150–1157 vol.2

Macrina T, Lee K, Lu R, et al (2021) Petascale neural circuit reconstruction: automated methods

Malnic B, Hirono J, Sato T, Buck LB (1999) Combinatorial receptor codes for odors. Cell 96:713–723. https://doi.org/10.1016/s0092-8674(00)80581-4

Mather JA (1995) Cognition in Cephalopods. In: Advances in the Study of Behavior. Elsevier, pp 317–353

McDonald AJ, Muller JF, Mascagni F (2002) GABAergic innervation of alpha type II calcium/calmodulin-dependent protein kinase immunoreactive pyramidal neurons in the rat basolateral amygdala. J Comp Neurol 446:199–218. https://doi.org/10.1002/cne.10204

Meinertzhagen IA (2019) Morphology of Invertebrate Neurons and Synapses. The Oxford Handbook of Invertebrate Neurobiology. https://doi.org/10.1093/oxfordhb/9780190456757.013.9

Meirovitch Y, Kang K, Draft RW, et al (2021) Neuromuscular connectomes across development reveal synaptic ordering rules. 2021.09.20.460480

Meirovitch Y, Mi L, Saribekyan H, et al (2019) Cross-Classification Clustering: An Efficient Multi-Object Tracking Technique for 3-D Instance Segmentation in Connectomics. pp 8425–8435

Messenger JB (1996) Neurotransmitters of cephalopods. Neurotransmitters of cephalopods 2:95–114

MICrONS Consortium, Bae JA, Baptiste M, et al (2021) Functional connectomics spanning multiple areas of mouse visual cortex. 2021.07.28.454025

Morgan JL, Berger DR, Wetzel AW, Lichtman JW (2016) The Fuzzy Logic of Network Connectivity in Mouse Visual Thalamus. Cell 165:192–206. https://doi.org/10.1016/j.cell.2016.02.033

Morgan JL, Lichtman JW (2020) An Individual Interneuron Participates in Many Kinds of Inhibition and Innervates Much of the Mouse Visual Thalamus. Neuron 106:468-481.e2. https://doi.org/10.1016/j.neuron.2020.02.001

Motta A, Berning M, Boergens KM, et al (2019) Dense connectomic reconstruction in layer 4 of the somatosensory cortex. Science 366:. https://doi.org/10.1126/science.aay3134

Packard A (1972) Cephalopods and Fish: The Limits of Convergence. Biological Reviews 47:241–307. https://doi.org/10.1111/j.1469-185X.1972.tb00975.x

946 Parsons TD, Sterling P (2003) Synaptic Ribbon: Conveyor Belt or Safety Belt? Neuron 37:379–
947 382. https://doi.org/10.1016/S0896-6273(03)00062-X

948 Pavarino E, Berger D, Kang K, et al (2019) mEMbrain: an interactive deep learning tool for
949 labeling and instance segmentation of EM datasets. [Poster]. Bernstein Conference,
950 September 17-18, Berlin, doi: 10.12751/nncn.bc2019.0083

951 Ramírez OA, Couve A (2011) The endoplasmic reticulum and protein trafficking in dendrites and
952 axons. Trends in Cell Biology 21:219–227. https://doi.org/10.1016/j.tcb.2010.12.003

953 Ronneberger O, Fischer P, Brox T (2015) U-Net: Convolutional Networks for Biomedical Image
954 Segmentation. In: Navab N, Hornegger J, Wells WM, Frangi AF (eds) Medical Image
955 Computing and Computer-Assisted Intervention – MICCAI 2015. Springer International
956 Publishing, Cham, pp 234–241

957 Ryan K, Lu Z, Meinertzhagen IA (2016) The CNS connectome of a tadpole larva of Ciona
958 intestinalis (L.) highlights sidedness in the brain of a chordate sibling. eLife 5:e16962.
959 https://doi.org/10.7554/eLife.16962

960 Saalfeld S, Fetter R, Cardona A, Tomancak P (2012) Elastic volume reconstruction from series
961 of ultra-thin microscopy sections. Nat Methods 9:717–720.
962 https://doi.org/10.1038/nmeth.2072

963 Sanders GD (1975) The Cephalopods. In: Corning W.C., Dyal J.A. & Willows A.O.D. (eds)
964 Invertebrate learning, Vol. 3. Plenium Press, New-York, pp 1-101.

965 Scheffer LK, Xu CS, Januszewski M, et al (2020) A connectome and analysis of the adult
966 Drosophila central brain. eLife 9:e57443. https://doi.org/10.7554/eLife.57443

967 Schmidt M, Derby CD (2011) Cytoarchitecture and ultrastructure of neural stem cell niches and
968 neurogenic complexes maintaining adult neurogenesis in the olfactory midbrain of spiny
969 lobsters, Panulirus argus. J Comp Neurol 519:2283–2319.
970 https://doi.org/10.1002/cne.22657

971 Schneider-Mizell CM, Gerhard S, Longair M, et al (2016) Quantitative neuroanatomy for
972 connectomics in Drosophila. eLife 5:e12059. https://doi.org/10.7554/eLife.12059

973 Schnell AK, Hanlon RT, Benkada A, Jozet-Alves C (2016) Lateralization of Eye Use in
974 Cuttlefish: Opposite Direction for Anti-Predatory and Predatory Behaviors. Front Physiol
975 7:. https://doi.org/10.3389/fphys.2016.00620

976 Shapson-Coe A, Januszewski M, Berger DR, et al (2021) A connectomic study of a petascale
977 fragment of human cerebral cortex. 2021.05.29.446289

978 Shigeno S, Andrews PLR, Ponte G, Fiorito G (2018) Cephalopod Brains: An Overview of
979 Current Knowledge to Facilitate Comparison With Vertebrates. Front Physiol 9:.
980 https://doi.org/10.3389/fphys.2018.00952

981 Shigeno S, Ragsdale CW (2015) The gyri of the octopus vertical lobe have distinct
982 neurochemical identities. J Comp Neurol 523:1297–1317.
983 https://doi.org/10.1002/cne.23755

Shomrat T, Feinstein N, Klein M, Hochner B (2010) Serotonin is a facilitatory neuromodulator of synaptic transmission and “reinforces” long-term potentiation induction in the vertical lobe of Octopus vulgaris. Neuroscience 169:52–64. https://doi.org/10.1016/j.neuroscience.2010.04.050

Shomrat T, Graindorge N, Bellanger C, et al (2011) Alternative Sites of Synaptic Plasticity in Two Homologous “Fan-out Fan-in” Learning and Memory Networks. Current Biology 21:1773–1782. https://doi.org/10.1016/j.cub.2011.09.011

Shomrat T, Turchetti-Maia AL, Stern-Mentch N, et al (2015a) The vertical lobe of cephalopods: an attractive brain structure for understanding the evolution of advanced learning and memory systems. J Comp Physiol A Neuroethol Sens Neural Behav Physiol 201:947–956. https://doi.org/10.1007/s00359-015-1023-6

Shomrat T, Turchetti-Maia AL, Stern-Mentch N, et al (2015b) The vertical lobe of cephalopods: an attractive brain structure for understanding the evolution of advanced learning and memory systems. Journal of Comparative Physiology A 201:947–956. https://doi.org/10.1007/s00359-015-1023-6

Shomrat T, Zarrella I, Fiorito G, Hochner B (2008) The Octopus Vertical Lobe Modulates Short-Term Learning Rate and Uses LTP to Acquire Long-Term Memory. Current Biology 18:337–342. https://doi.org/10.1016/j.cub.2008.01.056

Stern-Mentch N, Winters-Bostwick G, Belenky M, et al (2022) Neurotransmission and neuromodulation systems in the learning and memory network of Octopus vulgaris. Journal of Morphology n/a: https://doi.org/10.1002/jmor.21459

Turchetti-Maia A, Shomrat T, Hochner B (2017) The Vertical Lobe of Cephalopods—A Brain Structure Ideal for Exploring the Mechanisms of Complex Forms of Learning and Memory. The Oxford Handbook of Invertebrate Neurobiology. https://doi.org/10.1093/oxfordhb/9780190456757.013.29

Turchetti-Maia AL, Stern-Mentch N, Bidel F, et al (2018) A novel NO-dependent ‘molecular-memory-switch’ mediates presynaptic expression and postsynaptic maintenance of LTP in the octopus brain. bioRxiv 491340. https://doi.org/10.1101/491340

Turner GC, Bazhenov M, Laurent G (2008) Olfactory Representations by Drosophila Mushroom Body Neurons. Journal of Neurophysiology 99:734–746. https://doi.org/10.1152/jn.01283.2007

Turrigiano GG, Nelson SB (2004) Homeostatic plasticity in the developing nervous system. Nature Reviews Neuroscience 5:97–107. https://doi.org/10.1038/nrn1327

van den Pol AN (2012) Neuropeptide transmission in brain circuits. Neuron 76:98–115. https://doi.org/10.1016/j.neuron.2012.09.014

Verasztó C, Jasek S, Gühmann M, et al (2020) Whole-animal connectome and cell-type complement of the three-segmented Platynereis dumerilii larva. bioRxiv 2020.08.21.260984. https://doi.org/10.1101/2020.08.21.260984

1022 Vitti JJ (2013) Cephalopod Cognition in an Evolutionary Context: Implications for Ethology.
1023 Biosemiotics 6:393–401. https://doi.org/10.1007/s12304-013-9175-7

1024 Wadell H (1935) Volume, Shape, and Roundness of Quartz Particles. The Journal of Geology
1025 43:250–280

1026 Weigel AV, Chang C-L, Shtengel G, et al (2021) ER-to-Golgi protein delivery through an
1027 interwoven, tubular network extending from ER. Cell 0:
1028 https://doi.org/10.1016/j.cell.2021.03.035

1029 West MJ, Gundersen HJG (1990) Unbiased stereological estimation of the number of neurons
1030 in the human hippocampus. Journal of Comparative Neurology 296:1–22.
1031 https://doi.org/10.1002/cne.902960102

1032 White JG, Southgate E, Thomson JN, Brenner S (1986) The Structure of the Nervous System of
1033 the Nematode Caenorhabditis elegans. Philosophical Transactions of the Royal Society
1034 B: Biological Sciences 314:1–340. https://doi.org/10.1098/rstb.1986.0056

1035 Winters GC, Polese G, Di Cosmo A, Moroz LL (2020) Mapping of neuropeptide Y expression in
1036 Octopus brains. J Morphol 281:790–801. https://doi.org/10.1002/jmor.21141

1037 Witvliet D, Mulcahy B, Mitchell JK, et al (2021) Connectomes across development reveal
1038 principles of brain maturation. Nature 596:257–261. https://doi.org/10.1038/s41586-021-
1039 03778-8

1040 Witvliet D, Mulcahy B, Mitchell JK, et al (2020) Connectomes across development reveal
1041 principles of brain maturation in C. elegans. bioRxiv 2020.04.30.066209.
1042 https://doi.org/10.1101/2020.04.30.066209

1043 Young JZ (1979) The nervous system of Loligo. V. The vertical lobe complex. Philosophical
1044 Transactions of the Royal Society of London 285:311–354

1045 Young JZ (1995) Multiple matrices in the memory system of Octopus. In: Cephalopod
1046 Neurobiology. Oxford University Press, Oxford

1047 Young JZ (1971) The anatomy of the nervous system of Octopus vulgaris. Clarendon Press

1048 Zarrella I, Ponte G, Baldascino E, Fiorito G (2015) Learning and memory in Octopus vulgaris: a
1049 case of biological plasticity. Current Opinion in Neurobiology 35:74–79.
1050 https://doi.org/10.1016/j.conb.2015.06.012

1051 Zheng Z, Lauritzen JS, Perlman E, et al (2018) A Complete Electron Microscopy Volume of the
1052 Brain of Adult Drosophila melanogaster. Cell 0: https://doi.org/10.1016/j.cell.2018.06.019

1053 Zhu PC, Thureson-Klein Å, Klein RL (1986) Exocytosis from large dense cored vesicles outside
1054 the active synaptic zones of terminals within the trigeminal subnucleus caudalis: A
1055 possible mechanism for neuropeptide release. Neuroscience 19:43–54.
1056 https://doi.org/10.1016/0306-4522(86)90004-7

1057

1058

1059

1060 **Methods**

1061 **Tissue preparation**

1062 A mature wild *Octopus vulgaris* was collected by local fisherman on the Israeli Mediterranean coast and
1063 was held in artificial seawater in an individual aquarium for a few days. As previously published (Shomrat
1064 et al. 2011), the animal was deeply anesthetized in seawater containing 55 mM $MgCl_2$ and 2% ethanol. The
1065 supraoesophageal mass was removed through a dorsal opening of the cranium (Young 1971) and then
1066 quickly sliced into 1 mm sagittal sections using a mouse matrix brain slicer and double- edged razor blade.
1067 Three slices containing the vertical lobes were obtained and immersed in fixative solution (20:1 ratio).

1068 **Fixation**

1069 Because the preservation of the ultrastructure is a central requirement of a connectomics study, 3 fixations
1070 protocol were tested. The 3 solutions were chosen for their various aldehyde concentrations and tonicity as
1071 well as their previous use with octopus or other marine invertebrate tissue preparations for electron
1072 microscopy. Each slice was immersed in one of the following:
1073 Fixative #1 (Kier 1996): 3 % glutaraldehyde, 0.065 M phosphate buffer(PB), 0.5% tannic acid and 6%
1074 sucrose for 12 hr at 4°C.
1075 Fixative #2 (Feinstein et al. 2011): a mixture of 3 % glutaraldehyde and 4 % paraformaldehyde
1076 formaldehyde in artificial seawater for 4 hr at room temperature (RT).
1077 Fixative #3 (Schmidt and Derby 2011): 5% glutaraldehyde in 0.1 M PB containing 15% sucrose for 4 hr at
1078 RT.
1079 After fixation, the slices were rinsed in 0.1M PB 4 × 30 minutes, then transferred to chilled 0.065 M
1080 phosphate buffer with 1% glutaraldehyde and 6% sucrose and stored at 4°.

1081 We chose fixative #1 for the volumetric reconstruction, constituting the 'large connectomics dataset'
1082 (4nm/px, 200 ns/px), due to good preservation of the macroelements (*i.e.,* cell body) and ultrastructure (*e.g.,*
1083 mitochondria, postsynaptic density, various types of synaptic vesicles, etc.) as well as the high contrast
1084 between elements. Fixative #3 showed poor preservation of the macroelements but greater expansion (more
1085 extracellular space) and overall better fine ultrastuctural preservation. Accordingly, this fixative was used
1086 to generate a small 'high-magnification dataset' (1nm/px, 2 μs/px) to examine possible synaptic
1087 specialization and the synaptic vesicles at the sites of LTP generation in the VL (Hochner et al., 2003,
1088 Shomrat et al., 2011).

1089 **EM staining**

1090 The samples were stained with a modified *en bloc* staining protocol that was developed by Hua et al. (2015)
1091 for volumetric EM imaging. Before staining, the chemically fixed tissues were rinsed 3 times for 20 min
1092 each in 150mM sodium cacodylate buffer (pH 7.4). The tissues were then stained in 2% w/v
1093 OsO4 buffered with 150mM cacodylate for 2 hours. After being rinsed 3 x 20 min in cacodylate buffer, the
1094 tissues were immersed in 1.5% w/v potassium ferrocyanide buffered with cacodylate for 4 hours. The
1095 tissues were rinsed in deionized water for 3 x 20 min and then incubated in filtered 0.5% w/v
1096 thiocarbohydrazide aqueous solution for 1.5 hours. The tissues were then rinsed in deionized water for 3 x
1097 20 min and stained again with 2% w/v OsO4 aqueous solution for 3 hours. After the second osmication, the
1098 tissues were rinsed in water for 3 x 20 min and transferred to 1% w/v uranyl acetate aqueous solution which
1099 was wrapped in aluminum foil to protect from light for overnight staining (approx.12 hours, RT). On the
1100 next day, the samples had a final rinse in water and were then dehydrated through 25%, 50%, 75%, 100%,
1101 100% acetonitrile solution for 20 min each into pure acetonitrile. The dehydrated samples were infiltrated
1102 with 25% EPON:acetonitrile for 6 hours, 50% EPON:acetonitrile for 12 hours, 75% EPON:acetonitrile for
1103 12 hours, 100% EPON for 12 hours, 100% EPON for another 12 hours. The fully infiltrated samples were
1104 placed in a flat embedding mold and incubated in a 60°C oven for two days.

1105 **Collection of serial ultrathin sections using an automated tape-collecting ultramicrotome (ATUM)**

1106 The block face of the sample cylinder was trimmed into a 1 × 1 mm square containing the vertical lobe. 30
1107 nm thin sections for the 'connectomics dataset' and 40nm sections for the 'high magnification dataset' were
1108 cut using a Leica ultramicrotome and collected on a home-built automated tape collecting system using a
1109 plasma-treated polyamide 8 mm wide tape (Kapton, Sheldahl) that was carbon-coated (Hayworth et al.
1110 2014). On collection of the sections, the tape was cut into strips, and these were mounted on 100 mm silicon
1111 wafers. The connectomics dataset was composed of 7 wafers, between 115-140 sections per wafer, (total
1112 892 sections), while the high magnification dataset was composed of a single wafer of 83 sections.

1113 **EM imaging**

1114 For the connectomics dataset the sections were first mapped at low resolution (**Figure 2A)** and the EM
1115 image stack was aligned by Fiji's plugin "Linear Stack Alignment with SIFT" to form a coherent 3D EM
1116 volume. The VL region free from large cracks in the tissue was chosen for high resolution imaging. The
1117 sections on the wafer were cleaned while in the Magellan microscope using the FEI-supplied plasma
1118 system. A FEI Magellan Scanning Electron Microscope (Thermofisher Scientific) equipped with custom
1119 image acquisition software (WaferMapper, Hayworth, Morgan et al. 2014) was used for high resolution
1120 imaging. A backscattered electron detector in long working distance mode with a ~3.2 NA current at 7 kev
1121 incident electron energy and a dwell time of 200 ns/px was used for imaging at 4 nm/px. For each section
1122 we obtained a 4 by 6 montage of image tiles (each tile was a 16000 x 16000-pixel image). At the end of

each imaging run, out of focus images were manually identified and retaken. Artefacts such as dirt, lead precipitates, wrinkles or even large folds were seen on many sections and severely damaged sections were removed from the total stack. This resulted in 51 sections missing from the 892 sections. However, the occurrence of serious damage in adjacent sections was rare, allowing confident tracing of the elements.

Image stitching and alignment

The stitching and alignment of the dataset were performed using a method inspired by Saalfeld et al (2012). Each step was parallelized over image tiles and sections. The single-beam electron microscope produced high resolution image tiles sized 16,000x16,000 pixels whose precise location relative to one another was not known at the nanometer level. Hence, stitching these tiles together required using image information. We stitched these image tiles for each of the 892 sections. The process consisted of a coarse-grained stitching followed by fine-grained stitching. The coarse-grained stitching performed a per-tile affine transformation, setting the tiles roughly in their final position. SIFT features (Lowe 1999) were computed for pixels up to 2,400 from the tile boundary. The features of the overlapping tiles were compared and matched to find point correspondences. To remove outliers of incorrect correspondences, the RANSAC algorithm (Fischler and Bolles 1981) was used, optimizing for rigid transformations. Finally, the tiles' affine transformation was optimized by minimizing the sum of squared roots of all correspondences.

To achieve better alignment and compensate for minor non-linear deformations in imaging, a fine-grained stitching was performed after the coarse-grained stitching. A triangular mesh was laid on each tile and a 1x1 µm2 area around each mesh vertex overlapping with an adjacent tile was cropped. The cropped patch was matched against a transformed cropped area of the neighboring tile of size 2x2 µm2. The 2D elastic optimization algorithm described in Saalfeld et al. (2012) was used to minimize the distances of the matches.

We applied a custom-made 3D alignment algorithm to obtain an image stack of all 892 sections. Once all the sections were stitched as described above, correspondences between adjacent sections were detected. The first step consisted of coarse features detection and matching, and subsequently patch matching in small regions. The matching was performed between all section pairs separated by at most one section (hence considering matches between non-adjacent sections). Coarse features were obtained from the stitched sections. The features were detected using the OpenCV SimpleBlobDetector ("OpenCV: cv:SimpleBlobDetector Class Reference" n.d.). The detector searched for circular blobs that typically corresponded to blood cells, mitochondria and axonal cross-sections. Features were defined using a SIFT descriptor (Lowe 1999). After matching the features of each pair of sections, RANSAC filtered out wrong matches, from which an affine transformation between the sections was computed. In the second step, fine-grained patch matching at half resolution was performed. A triangular mesh was laid on the sections and a

1.6x1.6 μm^2 area around each mesh vertex was cropped, followed by cross-correlation search against a transformed cropped area of the neighboring section of size 4x4 µm2. The valid cross-correlation matches were then used as an input to a 3D elastic optimization algorithm based on Saalfeld et al. (2012) which minimizes the cross-layer distance of the matches while preserving the 2D structure of the sections.

Semi-automatic segmentation: mEMbrain

To segment the aligned image stack (892 sections, volume 2.7 million μm^3; **Figure 1B**), we applied an automated reconstruction pipeline to the volume using a machine learning reconstruction pipeline (Lee et al. 2017; Meirovitch et al. 2019). The inputs to this pipeline required fully annotating the image stacks of 4 manually picked volumes (image stacks ranged in volume from 21.6 to 153 μm^3; **Figure 1-supplement 3**), which served as ground truth for training the artificial neural network. The annotation of this ground truth labeled two different categories: intracellular space, excluding cellular membranes (category 1), or any combination of cellular membrane and ECS (category 2). We leveraged the mEMbrain software package implemented in MATLAB (Pavarino et al. 2019) to obtain a first template of the cellular processes. This computation included training a deep neural network (Unet; Ronneberger et al., 2015) to classify pixels according to the two categories (accuracy above 93%) and produce a 2-dimensional instance segmentation of the individual cross-sections of all cellular compartments using Watersheds (Pavarino et al. 2019). We used custom code to merge colored neuronal cross-sections across slices of the image stack if adjacent cross-sections matched in shape or if adjacent processes had sufficient overlapping cytoplasm far from any cellular membrane. Applying this conservative merging resulted in a 3-dimensional representation of object instances that each rarely overlapped two distinct neuronal or glial processes, and often the splitting of complete neuronal processes into several segmented objects. In most cases, however, the 2-D cross sections were lawfully (fully) segmented into one object and after conservative agglomeration procedure based on shape matching these objects were correctly agglomerated over a few consecutive sections. We also applied 3D agglomeration procedures including mean affinity agglomeration suggested by Lee et al. (2017) and Meirovitch et al. (2019). However, due to membrane breaks these procedures often resulted in merge errors that were hard to manually proofread and hence this agglomeration was not included in the circuit analysis. We found the cause of the merge errors to be associated with specific cellular and compartment types, including the shafts of the large neurons and many synaptic boutons. Because such preparation artifacts severely affected the quality of our fully automated reconstruction, we combined the automated segmentation with manual methods described below.

Membrane-constrained ML-aided reconstruction.

To facilitate manual reconstruction we used the mEMbrain package (Pavarino et al. 2019) implemented in MATLAB (Mathworks) together with VAST (Volume Annotation and Segmentation Tool

1189 (https://software.rc.fas.harvard.edu/lichtman/vast/, Berger et al., 2018). Using U-net architectures of deep
1190 neural networks (Ronneberger et al. 2015) mEMbrain computed the boundaries of all cellular processes,
1191 scoring the likelihood (0 to 1) that pixels belonged to intracellular space (category 1) or not (category 2).
1192 mEMbrain arranged these scores into a volume of membrane probabilities consistent with the EM image
1193 stack layer in VAST, which allowed tracing cellular processes aided by the pre-computed membrane
1194 probabilities. We constrained the tracing to the membrane probabilities layer generated by mEMbrain using
1195 the "constrained painting" function in VAST, which restricted the tracing to connected components of
1196 pixels far from cellular membranes. This ML-aided tracing allowed the annotator to ignore the location of
1197 the cellular membranes and work in a skeletonization mode if the initial painting stroke overlapped
1198 intracellular space. Tests on small volumes suggested a ~5-10x faster annotation in this mode than manual
1199 painting without constraints, while retraining the accuracy of careful pixel annotation. This membrane-
1200 constrained ML-aided reconstruction was used for the 516 cells described and studied morphologically here
1201 (**Figure 1C**).

1202 **Node-based agglomeration of 3D compartments**

1203 We also converted the automated neuron reconstruction IDs into a VAST image stack layer holding the
1204 identities of ~$16x10^6$ objects to allow even faster semi-automated reconstruction of processes. In this
1205 procedure the annotator used the automatic reconstruction by iteratively agglomerating 3D objects that were
1206 found to belong to a single cellular process. This was done using VAST's "Tool Layer" functionality which
1207 we mapped to the automated segmentation layer and to an additional annotation layer that represented the
1208 annotator's manually made skeletons. The annotator placed single nodes within the objects segmented by
1209 the automated reconstruction pipeline; together the collection of nodes of a single skeleton defined the
1210 agglomeration of all objects straddled by the nodes into a single proofread cell. This membrane-constrained
1211 ML-aided reconstruction was used to quickly reconstruct all the synaptic partners of one LN (**Figure 7C**)
1212 and one AF (**Figure 9 - figure supplement 1**).

1213 **Criteria for cell classification**

1214 Our morphological reconstruction included 516 cells segments and a wiring length of more than 12.8 cm.
1215 Only neurons that were sufficiently contained within the reconstructed volume were classified. Processes
1216 that could not be followed across the volume or were not wholly contained within it were considered orphan
1217 fragments and fell into the 'unmarked category' with other uncharacterized profiles.

1218 1. Afferent axons

1219 Classified as afferent axons were processes of constant radius (as opposed to dendrites that often taper),
1220 with exclusively presynaptic boutons filled with synaptic vesicles smaller than 60 nm and with no
1221 connection to a cell body. Two processes met these features: the SFL axons (see Results; **Figure 3** and the
1222 CIN (see Results; **Figure 8**). The SFL axons were classified according to several established criteria (Gray
1223 and Young 1964; Gray 1970; Young 1971): the axon projected into the VL lobule within the outer zone of
1224 the neuropil, made *en passant* synapses with AM neurons and at the ultrastructural level their varicosities
1225 showed an electron-lucent cytoplasm with average synaptic vesicle size of 59.7 ± 1.5nm, and numerous
1226 round mitochondria. Unlike the SFL, CIN were found in the SFL and in the neuropil, displayed the smallest
1227 vesicles in our dataset (38.2 ± 0.9 nm) and synapsed exclusively with clear postsynaptic profiles.
1228 Additionally, CIN fibers showed a high concentration of neurofilaments which ended where the synaptic
1229 vesicles appeared (Gray 1970). The high neurofilament content of these processes led Gray (1970) to
1230 suggest that these were pain fibers. Both afferents could be easily identified with only electron micrographs.

1231 2. VL Interneurons

1232 Neurons were classified as VL interneuron if they received input from the SFL and/or were previously
1233 described as intrinsic to the lobes. All partners of the SFL axons were the AM cells (Gray and Young
1234 1964; Gray 1970; Young 1971). However, we discovered two types of AMs: SAM and CAM (see Results;
1235 **Figure 6**). The SAMs showed a single inwardly directed trunk that cannot be defined either as axon or
1236 dendrite. Additionally, their ultrastructural signature was easily identifiable through the presence of
1237 synaptic vesicles (49.5 ± 1.3 nm) along the length of this trunk and the presence of specific ultrastructural
1238 components such as cisternae and the transport endoplasmic reticulum at every presynaptic site. Unlike the
1239 SAM, the CAM displayed a strict segregation between a dendritic compartment located within the SFL
1240 tract and their axonal process within the neuropil. Their dendritic tree was lightly or heavily branched, with
1241 one or multiple axons arising from it. Their dendritic arborizations displayed a classical electron-lucent
1242 postsynaptic profile filled with polyribosome. Unlike the SAMs, the CAM presynaptic sites in the neuropil
1243 displayed a clearer cytoplasm with no specific ultrastructure and smaller vesicles than the SAMs (42.6 ±
1244 1.1 nm).

1245 We also observed putative interneurons displaying a bifunctional neurite, with both pre- and postsynaptic
1246 sites identified (**Figure 1-figure supplement 3A**). Previously undescribed and poorly represented in our
1247 dataset and apparently poorly involved in the major cell network, all such cells were considered as
1248 unmarked cells in the data analysis.

1249 3. Efferent Fibers

1250 Only the LNs fell into this category. Their cell bodies (diameter > 15 µm; n=14) lay mostly in the inner
1251 zones of the cortex and their large trunks ran radially into the neuropil (see Results; **Figure 7**). While most
1252 of the LNs were poorly contained in the reconstructed volume, some gave off dendritic collaterals within
1253 the SFL tract area where they were solely postsynaptic to the SAMs and unmarked process. Their dendrites
1254 showed a variable diameter along their length and displayed a typical clear postsynaptic profile. In the
1255 neuropil, we classified all clear postsynaptic profiles with convoluted arborizations heavily innervated by
1256 the AMs as LN processes.

1257 4. Neuromodulatory neurons

1258 Based on known invertebrate modulatory synapses, processes were classified as modulatory if they
1259 contained mostly large vesicles (>60 nm), either dark or clear. We distinguished two types of
1260 neuromodulatory processes (see Results; **Figure 9**). First, the ascending fibers (AF) with a distinctive
1261 morphology - a menorah –shaped tree climbing from the neuropil to the cortex while intermingling with
1262 SAM trunks. Along their length the AF displayed boutons filled either with dense core vesicles (AF-Nm)
1263 and an average size of 74.9 ± 1,6 mm or a mix of smaller vesicle types that could be round, flattened or
1264 irregularly shaped (AF-mix). Various subtypes of AF-mix were observed. The AF-Nm neurons were
1265 heavily innervated by the SAMs without any sign of presynaptic activity. In contrast, the AF-mix were
1266 innervated to lesser extend by the SAMs and displayed some presynaptic sites as well as occasionally
1267 reciprocal contacts.

1268 The second type were neuromodulatory fibers (NMs) which were dispersed more globally in the VL
1269 neuropil and within the SFL tract and lacked a general orientation. Several subtypes were characterized by
1270 the homogeneity of the vesicle types found along their length. Most of their boutons lacked any sign of
1271 synaptic connection but the few pre- or postsynaptic sites observed were unorthodox. These NM processes
1272 displayed the largest vesicles in the entire dataset with diameters up to 200 nm (mean 96.3 ± 3.5 nm) within
1273 their bouton and an accumulation of much smaller vesicles was observed at their rather rare presynaptic
1274 sites.

1275 5. Glia

1276 Cells were classified as glia if they showed clearly distinguishable gliofibrils (Gray, 1964) and/or did not
1277 receive any synapses. At least two types of protoplasmic glia were identified (**Figure 1-figure supplement**
1278 **3C**). (1) radial glia (Young, 1971) were full of gliofibrils and characterized by long radial processes and
1279 arborizations infiltrating the neuronal cell cortex. These cells appear to isolate neuronal types from each
1280 other. (2) The astrocyte-like glia had many gliofibrils within their processes, which showed an increased
1281 tortuosity densely infiltrating the SFL tract. Here they appeared to wrap distinct synaptic areas. Through

1282 repeating folds this cell type appears to maximize self-contacts characterized by apposition of their
1283 membranes and accumulation of electron dense materials on both sides, possibly sites for protein exchange.
1284 One astrocyte-like cell with its cell body located near a cell island was partially reconstructed; it covered
1285 an extensive area within the SFL tract. (3) Fibrous glia with cell bodies in the inner cortex were also
1286 observed; these did not receive any synapses in the reconstructed volume.

1287 6. Progenitor-like cells

1288 Cells were classified as progenitor-like only if their cell body was reconstructed (**Figure 1-figure**
1289 **supplement 3B**). These cells were nested in each other in the inner cortex forming a type of horizontal
1290 layer. There were at least two types of cells in this arrangement. First, the base was formed by elongated
1291 cell bodies whose nuclei showed bumpy irregular membranes often with nuclear folds. These cell bodies
1292 appeared to have very small projections, and, like the glia, they lacked synaptic connections. Above these
1293 elongated cells were more classically spherical cell bodies which appeared somewhat "immature." Their
1294 trunks, extending radially into the neuropil, often lacked synaptic connection and terminated early with
1295 filopodia typical of axon growth cones. Their fibers were rich in grayish filaments that could be filamentous
1296 actin, suggesting that this may be a site of plastic reorganization. Because of the similarity of this
1297 arrangement with neurogenic niches observed in the mammalian dentate gyrus of the hippocampus and
1298 the subventricular zone, we termed these cells "progenitor-like cells." We saw no sign of cell division.

1299 **Identification and analysis of synapses**

1300 Chemical synapses were identified by features common to invertebrate synapses - the presence of a cluster
1301 of synaptic vesicles (sv) or 'cloud' associated with a lightly active zone near the presynaptic membrane
1302 (Gray 1970; White et al. 1986; Ryan et al. 2016; Zheng et al. 2018; Meinertzhagen 2019; Witvliet et al.
1303 2020). Synapses were annotated if the accumulation of sv persisted through at least 3 sections in a row
1304 (90nm). We distinguished between traditional chemical synapses (fast transmission) with 30-60nm sv and
1305 synapses of modulatory neurons with mostly large vesicles (Witvliet et al. 2020). Consistent with previous
1306 studies (Gray and Young 1964; Gray 1970), we did not find evidence of electrical connections (gap
1307 junction) or any clear postsynaptic density (PSD) at any chemical synapse within the vertical lobe.
1308 However, in the connectomics dataset we observed a rather global membrane thickening at synaptic sites.
1309 This may be partly due to a lack of resolution and the observed global overstaining.

1310 The high magnification dataset was used to confirm the synaptic nature of the connections observed in the
1311 connectomics dataset and the absence of PSD. The absence of PSD made it difficult to annotate polyadic
1312 varicosities (one cluster of vesicles could be associated with two postsynaptic targets). In ambiguous cases
1313 only the most likely partners were identified (larger surface contact), leading to a likely underestimation of

1314 the overall number of synapses. Because most of the cells were not fully contained in the reconstructed
1315 volume, it was not possible to assess the full collection of synapses between a given presynaptic and
1316 postsynaptic neuron. For this reason, we refer to "synaptic site," a single anatomical release site or a single
1317 synapse. Multiple synaptic sites from the same cell were classified as a single input. Additionally, because
1318 cells had different lengths of arbor in the reconstructed volume, we expressed most of the results as synaptic
1319 fraction and number of synaptic sites per 100 µm.

1320 Although multiple annotators would have been ideal, due to project constraints and the difficulty of training
1321 people in an entirely new dataset where most synapses are being described for the first time, all synaptic
1322 annotations were made by a single annotator, giving consistency across annotations.

1323 **Clustering of cells based on connectivity**

1324 As described above, the reconstructed cells and processes of the vertical lobe were classified based
1325 primarily on morphological criteria. We combined this classification with unsupervised clustering to obtain
1326 a visual summary of the connectivity patterns found in the lobe. First, we produced a cell type wiring
1327 diagram connecting the 7 main cell types (**Figure 2**). The nodes of this graph comprise cell types and the
1328 weighted edges between pairs of cell types represent the number of synapses between the processes that
1329 belonged to these cell types. We used a spring model to minimize the distances between the pairs of nodes
1330 (representing pairs of cell types) that corresponded to a relatively larger number of synapses (Fruchterman
1331 and Reingold 1991). This diagram revealed that synapses within a cell type are rare in the vertical lobe
1332 (mainly in ascending fibers; see Results). In addition, visually inspecting this diagram clarified that the
1333 connectivity was highly structured and far from an "all-to-all" connectivity. Each cell type was connected
1334 to a small number of other cell types (see Results). This observation led us to consider the common inputs
1335 and common outputs of specific processes (described below).

1336 We also discovered that besides these uncommon within-type synapses, there were no connectivity cycles
1337 in the cell-type wiring diagram. This observation led us to analyze the possible cycles in the wiring diagram
1338 while considering individual processes (see above Criteria for cell classification). We then used an
1339 unsupervised approach to visualize the connectivity among individual processes (**Figure 2 – figure**
1340 **supplement 1**). This was done by considering the adjacency matrix $\mathbf{A_{NxN}}$ whose **(i,j)** entries represent the
1341 number of synapses from the presynaptic neuron **i** to the postsynaptic neuron **j,** considering **N** neurons
1342 (**N**=362). As specific groups of cells tended to synapse into other specific subsets of cells, a stereotypy
1343 observed from the cell-type diagram, we considered the number of shared inputs and shared outputs
1344 between individual processes, mathematically represented by the common output and common input
1345 symmetric matrices, **A*A'** (**presynaptic**) and **A'*A** (**postsynaptic**), respectively. The presynaptic matrix
1346 represents how many common targets exist for pairs of neurons and the postsynaptic matrix represents how

many common inputs exist for pairs of neurons. To visualize the tendencies of neurons to share inputs or outputs, we considered the matrix **A*A'+ A'*A** which sums for every pair of neurons the number of shared inputs and outputs, using subspace embedding (Koren 2005) and 100 dimensions, heuristically picking a dimension that yielded sufficient separation between individual nodes (nearby dimension produced visually similar outcomes). This embedding of the neurons in the plane resulted in a close positioning with other neurons with a similarity of inputs and outputs (summed). The position of the entire layout and its orientation are arbitrary and not used to derive biological observations. To combine the cell type- and neuron-based diagrams, each neuron was located based on its type diagram shifted by its location in the neuron-based wiring diagram (**Figure 2**).

Analysis of feed-forwardness

The cell type-based wiring diagram analysis revealed that connectivity cycles were rare and information flowed in one direction among populations of cells belonging to different cell types (**Figure 2**). To determine if there were cyclic synaptic information flows in the reconstructed circuit at the level of individual neurites we used graph algorithms that detect directed cycles in directed graphs. Topological sorting algorithms (Barth et al. 2004) that determine a linear order in cycle-free directed graphs were used to detect cycles in the graph. A topological sorting is a sequence of nodes each of which is possibly connected only to nodes proceeding in the list. Hence, we inspected all the edges in the topological sorting that went backward. We found a few edges (n= 4) that violated the forwardness of the circuit and each of these cases was related to a reciprocal synapse between a pair of nodes associated with a single synaptic site between the cells. We also calculated the probability of observing this level of forwardness in random graphs that agreed with the wiring diagram, but in which the direction of synaptic transmission was randomized. This showed that the level of forwardness in the data is unlikely to occur by chance ($p<0.05$).

Classification of cell types from cell body morphology

Our reconstruction revealed that the SAM, CAM, and LN cell bodies lay in the VL cortex along with several other cell types: glia, progenitor-like and mix cells (Others; **Figure 1 – supplement 4**). We noticed, consistently with early studies, that the LNs had extremely large cell bodies and that the newly discovered CAMs tended to have a slightly larger cell bodies than the SAMs. We tested whether these observations could be used to classify cell types directly from the morphology of their cell bodies. We used 110 cells whose somata were contained in the volume and their processes were distinctly characterized in the neuropil by an expert annotator: 7 LNs (6.36%), 69 SAMs (62.73%), 16 CAMs (14.55%) and 18 others (16.36%). The selection of this subset of cells was agnostic to the details of the classification process described here. For each of these cells we considered the volume of the cell body as the number of annotated voxels multiplied by the volume unit of a voxel, and the volume, surface area and sphericity (Wadell 1935) of the

ellipsoid best matching the geometry of the cell body. Ellipsoid approximations were computed from the eigenvectors and eigenvalues of the covariance matrix of the voxel coordinates of the cell bodies.

Our tests showed that the information gained from these ellipsoids were sufficiently discriminative and hence these 3 parameters (volumes, surface area and sphericity) were used for further analyses. Support Vector Machines (SVMs) were used to train, cross-validate and predict the 3 main cell classes found in the cortex: LN, SAM and CAM and a 4th class, Other, to represent the seemingly small number of other cell types in the cortex (including glia, progenitor cells and possibly other cells of scarce representation). The min, max, mean and std of these parameters were computed for each class as well as the training accuracy (see Results).

In addition, a set of 49 cells (each cell was annotated twice) was used to determine the accuracy of the SVMs and for leave-one-out cross validation (see Results). Once the SVM model was determined from the training set, it was applied to a test set, comprising 1447 cells, that were densely annotated in the cortex (using mEMbrain and VAST as described above). The number and percentage of each of the 4 classes were calculated (see Results; **Figure 4**).

Wire-length calculation

To calculate the length of the processes (see Results; **Figure 2**), we used a thinning algorithm to map each volumetric object into a skeleton and used graph theory algorithms to measure the total length of skeletons. This was done by calculating the graph distance between skeleton nodes representing the end of the volumetric object (a leaf; a node that is connected to at most one other node, e.g., of the last node in a branch terminating at a synapse) and skeleton nodes representing branching (nodes that are connected to more than two other nodes, e.g., a branching point of a dendrite-like structure or axonal branching). The distances between adjacent skeletal nodes were defined using the Euclidean distance between the voxels in the 3D 26-neigberhood mask (a 3x3 cube around each voxel). We then summed up all these distances to measure the wire-length of each process. Occasionally the thinning algorithm produces a biologically meaningless cycle due to topological holes in the annotated objects (either biological or imperfect annotation). We guaranteed that only the shortest paths between special skeletal nodes (bifurcations and leaves) were used for the wire-length calculation using minimum distance graph algorithms between leaf and bifurcation nodes.

SFL bouton volume calculation

Synaptic boutons are morphologically easy to identify, and they were accordingly individually segmented to allow volumetric measurements (see Results; **Figure 3**). Volumes of boutons were estimated from the voxel counts of each bouton. A *post hoc* exact permutation test for independent samples compared the

volumes of the SFL SB and SFL LB. The p-values were adjusted according to the sequential Bonferroni correction as described by Holm (1979).

Subcellular reconstruction

The geometry of the SFL large synaptic boutons and the postsynaptic structures they innervate were reconstructed at the subcellular level using the high magnification dataset (see Results; **Figure 5**). Neuronal elements of interest were manually segmented on VAST. The labeled images and metadata containing the labels were exported and processed externally or accessed through the VAST API. Vesicles showing a clear synaptic center in each section were counted by outlining intracellular space containing vesicles (see more information below). Mitochondria were identified by the presence of an inner membrane with visible cristae. Transport endoplasm, large electron-lucent tubular organelles, spanned the reconstructed volume and appeared to be a continuous structure present throughout the length of the AM trunk. They showed large swellings at the presynaptic site, particularly at the 'palm'. Discontinuous thin lucent tubular organelles that sometimes appeared as dark lines were annotated as 'cisternae' (Cis). It is not clear whether the Cis (up to 15 observed in one palm) were part of the larger endoplasmic reticulum network or were isolated entities.

Counting, modelling, and measuring vesicles

An annotator painted all individual vesicles of several compartments using distinct colors per compartment. Distinct colors were used to annotate the active zones. The center of mass and areas of the vesicle cross-sections were used to approximate the centers and spherical representations of individual vesicles, from which spherical 3D mesh representations were computed. Occasionally, several vesicles of the same compartment were overlapped spatially. This required us to use distance transforms and watersheds to achieve separation of vesicles. Vesicle counts were made only after they were separated in space. Due to the section thickness (30 nm), most of the vesicles were clearly appreciated in a single section, whereas only the largest vesicles (> 60nm diameter) may have had a strong signal in two adjacent sections. The annotator attempted to avoid overrepresentation of a vesicle, when possible, but since this task is not unambiguous our counts likely represent an upper bound. Extremely small vesicle-like structures were not annotated since it was assumed that these structures were likely represented in adjacent sections.

Rendering

For rendering of all the traced images, 3D surface meshes of labeled objects were generated from VAST using VastTools (written in MATLAB) and imported into 3D Studio Max 2020 (Autodesk Inc.) to generate 3D renderings of all the traced objects.

1444 **Data availability**

1445 The 'connectome dataset' is available at https://lichtman.rc.fas.harvard.edu/octopus_connectomes with 32
1446 nm resolution. 8 nm resolution will be provided, and the segmentation files added prior publication.